2019-02-01

Mineralogical constraints on the thermal history of martian regolith breccia Northwest Africa 8114

MacArthur, JL

10.1016/j.gca.2018.11.026
Geochimica et Cosmochimica Acta
Elsevier

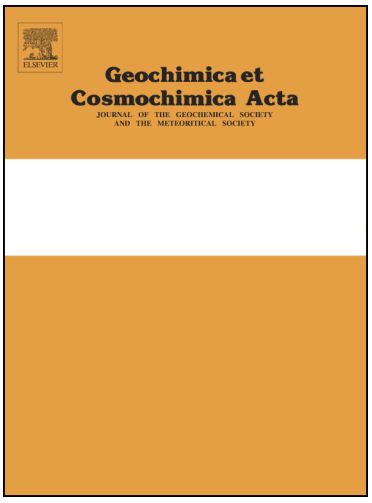

Mineralogical Constraints on the Thermal History of Martian Regolith Breccia Northwest Africa 8114

J.L. MacArthur, J.C. Bridges, L.J. Hicks, R. Burgess, K.H. Joy, M.J. Branney, G.M. Hansford, S.H. Baker, S.P. Schwenzer, S.J. Gurman, N.R. Stephen, E.D. Steer, J.D. Piercy, T.R. Ireland

PII: S0016-7037(18)30656-2
DOI: https://doi.org/10.1016/j.gca.2018.11.026
Reference: GCA 11021

To appear in: *Geochimica et Cosmochimica Acta*

Received Date: 8 March 2018
Revised Date: 15 November 2018
Accepted Date: 15 November 2018

Please cite this article as: MacArthur, J.L., Bridges, J.C., Hicks, L.J., Burgess, R., Joy, K.H., Branney, M.J., Hansford, G.M., Baker, S.H., Schwenzer, S.P., Gurman, S.J., Stephen, N.R., Steer, E.D., Piercy, J.D., Ireland, T.R., Mineralogical Constraints on the Thermal History of Martian Regolith Breccia Northwest Africa 8114, *Geochimica et Cosmochimica Acta* (2018), doi: https://doi.org/10.1016/j.gca.2018.11.026

Mineralogical Constraints on the Thermal History of Martian Regolith Breccia Northwest Africa 8114

J. L. MacArthur[1*]

J. C. Bridges[1]

L. J. Hicks[1]

R. Burgess[2]

K. H. Joy[2]

M. J. Branney[3]

G. M. Hansford[1]

S. H. Baker[4]

S. P. Schwenzer[5]

S. J. Gurman[4]

N. R. Stephen[6]

E. D. Steer[7]

J. D. Piercy[1]

T. R. Ireland[8]

[1]Leicester Institute for Space & Earth Observation, Dept. of Physics & Astronomy, University of Leicester, Leicester, LE1 7RH, UK. [*]Corresponding author jm650@le.ac.uk, +44 116 223 1045.

[2]School of Earth and Environmental Sciences, University of Manchester, Oxford Road, Manchester M13 9PL, UK.

[3]School of Geography, Geology and the Environment, University of Leicester, Leicester, LE1 7RH, UK.

[4]Dept. of Physics & Astronomy, University of Leicester, Leicester, LE1 7RH, UK.

[5]School of Environment, Earth and Ecosystem Sciences, The Open University, Milton Keynes, MK7 6AA, UK.

[6]Plymouth Electron Microscopy Centre & School of Geography, Earth & Environmental Sciences, University of Plymouth, Drake Circus, Plymouth, PL4 8AA, UK.

[7]Nanoscale and Microscale Research Centre, University of Nottingham, Nottingham, NG7 2RD, UK.

[8]Research School of Earth Sciences, The Australian National University, Canberra, ACT 2601, Australia.

ABSTRACT

Martian meteorite Northwest Africa (NWA) 8114 – a paired stone to NWA 7034 – provides an opportunity to examine the thermal history of a martian regolith and study near-surface processes and ancient environmental conditions near an impact crater on Mars. Our study reports petrographic and alteration textures and focuses on pyroxene and iron oxide grains. Some of the pyroxene clasts show exsolution lamellae, indicating a high temperature magmatic origin and slow cooling. However, transmission electron microscopy reveals that other predominantly pyroxene clasts are porous and have partially re-crystallised to form magnetite and a K-bearing feldspathic glassy material, together with relict pyroxene. This breakdown event was associated with oxidation, with up to 25% $Fe^{3+}/\Sigma Fe$ in the relict pyroxene measured using Fe-K XANES. By comparison with previous studies, this breakdown and oxidation of pyroxene is most likely to be a result of impact shock heating, being held at a temperature above 700 °C for at least 7 days in an oxidising regolith environment.

We report an approximate ^{40}Ar-^{39}Ar maximum age of 1.13 Ga to 1.25 Ga for an individual, separated, augite clast. The disturbed nature of the spectra precludes precise age determination. In section, this clast is porous and contains iron oxide grains. This shows that it has undergone the high temperature partial breakdown seen in other relict pyroxene clasts, and has up to 25% $Fe^{3+}/\Sigma Fe$. We infer that the age corresponds to the impact shock heating event that led to the high temperature breakdown of many of the pyroxenes, after consolidation of the impact ejecta blanket.

High temperatures, above 700 °C, may have been maintained for long enough to remobilise and congruently partially melt some of the alkali feldspar clasts to produce the feldspar veins and aureoles that crosscut, and in some cases surround, the oxidised pyroxene. However, the veins could alternatively be the result of a hydrothermal event in the impact regolith. A simple Fourier cooling model suggests that a regolith of at least five metres depth would be sufficient to maintain temperatures associated with the pyroxene breakdown for over seven days.

Low temperature hydrous alteration took place forming goethite, identified via XRD, XANES and FTIR. Comparing with previous studies, the goethite is likely to be terrestrial alteration pseudomorphing martian pyrite.

1 INTRODUCTION

Meteorite Northwest Africa NWA 8114 and its paired stones, NWA 7034, 7475, 7533, 7906, 7907, 8171, 8674, 10922, 11220, 11522 and Rabt Sbayta 003 (all known as the martian breccia) provide the first opportunity to study an impact breccia from the surface or near-surface of Mars. The presence of a trapped noble gas component similar to the modern martian atmosphere (Cartwright et al., 2014) together with oxygen isotope $\Delta^{17}O$ values that match and exceed those of other martian meteorites (Agee et al., 2013; Nemchin et al., 2014) confirm its martian origin. The martian breccia contains a wide range of crystalline clasts from low-Ca pyroxene to plagioclase and alkali feldspar, although olivine is largely absent. Iron oxides, Cl-apatite, chromite, and pyrite are also present in clasts and within the fine-grained matrix (Agee et al., 2013; Humayun et al., 2013; Muttik et al., 2014; Wittmann et al., 2015; Santos et al., 2015). Many of the pyroxene clasts exhibit exsolution lamellae with characteristics that indicate slow cooling rates and a range of parent rocks and formation depths, so must have developed prior to incorporation into the breccia (Leroux et al., 2016). There is also a diverse range of basaltic and alkaline igneous clasts (Santos et al., 2015) that were interpreted to be of impact melt origin (Humayun et al., 2013; Hewins et al., 2017).

Accretionary clasts and dust rims are also present in the martian breccia and may have formed in an ejecta plume (Wittmann et al., 2015). Melt spherules and clast-laden impact melt fragments have been identified in NWA 7533 (Humayun et al., 2013; Hewins et al., 2017), similar to melt clasts in NWA 7034 (Agee et al., 2013; Santos et al., 2015) and vitrophyre clasts in NWA 7475 (Wittmann et al., 2015). High Ni (1020 ppm) was measured in a vitrophyric clast confirming this as an impact melt product (Udry et al., 2014). Therefore, these polymict martian breccias have similarities to terrestrial suevite associated with base surges (i.e. density currents) (Wittmann et al., 2015; Hewins et al., 2017). Suevites are (usually polymict) impact breccias that contain inclusions of impact melt lithologies and the clastic matrix additionally contains melt particles (Stöffler and Grieve, 2007).

McCubbin et al. (2016) suggested that an impact process analogous to a pyroclastic fall deposit is responsible for the formation of the martian breccia samples, due to the clast size and shape distribution. The presence of meteoritic siderophiles (Ni, Ir) in the fine matrix have been taken to indicate a 5% (Humayun et al., 2013), or ~3% based on Ir and HSEs in the bulk rock (Wittmann et al., 2015; Goderis et al., 2016), component of carbonaceous chondrite material and provides evidence that this is a regolith breccia (Humayun et al., 2013). Regolith breccias are a subgroup of consolidated clastic impact debris that contain matrix melt and melt particles (Stöffler and Grieve, 2007).

Ejecta blankets around impact craters on Mars are gradually modified by heating, alteration and transport processes, leading to reprocessed rocks that have undergone multiple disruption and re-accumulation events (Melosh, 2011). Most impact ejecta do not travel more than two crater

diameters from the source, with small impacts regularly overturning the top centimetre of surface material and less frequent larger impacts excavating and disturbing deeper lying material in a "gardening" process (Melosh, 2011), so regolith is thought to represent the local upper crust and surface composition. Thus, the martian breccia provides an opportunity to constrain conditions that occurred at the surface and in the near-surface of the regolith around an impact crater on Mars.

The wide variety of ages found in the meteorite breccia suggests a complex history of its clast source terrains. Nyquist et al. (2016) found disturbed Rb-Sr systematics and a Sm-Nd isochron age of 4.42 ± 0.02 Ga interpreted as a "bulk" crystallisation age for the breccia components. This age is consistent with 4.3-4.4 Ga U-Pb ages obtained from zircons in monzonitic clasts or breccia matrix, whereas chlorapatite and some zircons yield younger U-Pb ages 1.35-1.7 Ga, possibly recording the effects of impacts that disturbed the Rb-Sr system (Humayun et al., 2013; Bellucci et al., 2015; McCubbin et al., 2016). Further high precision U-Pb ages of seven zircons yield ages of 4.4763 ± 0.0009 Ga to 4.4297 ± 0.0001 Ga (Bouvier et al., 2018). The latter may represent the formation of the breccia from ancient precursor materials (Wittmann et al., 2015; Nyquist et al., 2016; Leroux et al., 2016). The cosmic ray exposure age indicating the ejection event is suggested to be ~5 Ma (Cartwright et al., 2014).

Hydrated iron oxides have been identified in NWA 7034 (Muttik et al., 2014; Beck et al., 2015), and monazite-bearing apatite in the meteorite is thought to have required fluids and temperatures above 100 °C (Liu et al., 2016). The presence of hyalophane in veins in a spherule in paired rock NWA 7533 is consistent with hydrothermal activity (Hewins et al., 2017). NWA 7034 is the most oxidised known martian meteorite (Agee et al., 2013) as shown by the presence of maghemite and goethite (Gattacceca et al., 2014). These results suggest that this breccia, or components of it, might have experienced near-surface aqueous alteration. The high hydration of bulk NWA 7034 with ~6000 ppm water, shows two distinct δD components (Agee et al., 2013). While the high-temperature component +300 ‰ is most likely martian in origin, the low-temperature component with δD of -100 ‰ could reflect contamination by terrestrial water (Agee et al., 2013). A terrestrial origin for some of this hydration is likely, and NanoSIMS D/H analyses of δD of 10 ±85 ‰ show a terrestrial origin for Fe oxyhydroxides through alteration of pyrite (Lorand et al., 2015). Further studies of the water content of paired stone NWA 7533 estimated ~8000 ppm (Beck et al., 2015) although Remusat et al. (2015) found <3600 ppm of martian water, with ilmenite containing 2000 - 3600 ppm of water with δD between 1370 and 3130‰ and apatite containing 560 – 3050 ppm of water with δD between 250 and 2230‰.

Any martian hydrous alteration in the breccia might be consistent with what has been determined through NIR spectroscopy (CRISM, OMEGA) of impact craters from orbit, some of which have been hypothesized to have preserved long-lived hydrothermal systems in the near-surface (Poulet et al., 2005; Bibring et al., 2006; Mustard et al., 2008; Schwenzer and Kring, 2009; Marzo et al., 2010; Ehlmann et al., 2011a; Ehlmann et al., 2011b; Mangold et al., 2012a). These are more

commonly seen in and around Noachian and Hesperian aged impact craters but are thought to be rarer during the Amazonian (Turner et al., 2016).

We use a combination of CT scanning, STEM, EDX, EPMA and synchrotron Fe-K XANES, XRD, FTIR to characterise the different mineralogical stages recording NWA 8114's thermal evolution and interaction with water. Four individual clasts were separated for ^{40}Ar-^{39}Ar attempted age determinations. Our goal is to constrain the formation and thermal history of the parent rocks, characterise high temperature effects in the regolith from the impact-forming event and investigate any interaction with water that it has experienced.

1.1.1 Clast Nomenclature

As this breccia is the first of its type, different authors have used various descriptive terms from volcanic, rock and mineral terminology to describe clasts and features within it. Table 1 provides a summary of some of the main classifications and terms and how they correspond between authors and with this study.

2 METHODS AND SAMPLES

The 1.9 g main mass of NWA 8114 (Fig. 1) was found in 2013 and obtained by the University of Leicester, with classification reported by Ruzicka et al., (2015). The stone was split into two pieces. From the type specimen held at UL a polished thin section (A) (Fig. 2), two polished thick sections (B, C), a polished block (D), and a double-polished wafer (F) of NWA 8114 were prepared. Four clasts were physically separated from the NWA 8114 stone, and split, with one half of each clast for ^{40}Ar-^{39}Ar analyses at the University of Manchester, and the other fragments for complementary mineralogical studies.

2.1 SEM-EDX, EPMA and CT Scanning

Sections A, B, C, D, F were characterised using a Phillips XL30 environmental scanning electron microscope (ESEM) and a Hitachi S-3600N ESEM with Oxford INCA 350 EDX spectroscopy system at the Advanced Microscopy Centre UL. Back-scattered electron (BSE) images and normalised EDX spectroscopy element data for point analyses were obtained using an accelerating voltage of 20 kV and beam current of ~1.0 nA.

Standardised X-ray element maps of section C (Fig. 3) were generated using a JEOL 7001F FEG-SEM with Oxford Instruments X-Max 50 mm^2 energy dispersive spectroscopy (EDS) detector within Plymouth Electron Microscopy Centre at the University of Plymouth. EPMA data were obtained for pyroxenes and iron oxides in sections A, B, C using a Cameca SX100 at the Open University, with TAP, LTAP, LLiF, LPET and PET spectrometer crystals, a focused 1 μm beam, at an accelerating voltage of 20 kV and beam current of 20 nA. A detailed mineralogical map and modal mineralogy of section A (Fig. 2B) were obtained using a Quanta 600 ESEM with two Bruker EDS spectrometers at the University of Nottingham. An X-ray micro computerised tomography (CT) scan was taken of the remainder of the 1.9 g NWA 8114 main mass (after sections A-D were prepared, but before further material was consumed in preparing sections F) using a Nikon Metrology XT H 225 scanner at UL. This provides a 3D image at high resolution of the internal structure and the composition of the bulk sample, processed using *VG Studio Max* (version 3) software (VG, 2017). The voxel size was 8 × 8 × 8 μm.

2.2 FIB-SEM and TEM-STEM-EDX

An FEI Quanta 200 3D dual Focused Ion Beam (FIB-SEM) at UL was used to prepare wafers from specific regions of interest in the clasts, which were first capped with a ~150 nm thick protective Pt layer, following the methods of Changela and Bridges (2010). The Ga^+ ion beam milled wafers measuring 5 × 15 μm and 50–100 nm thick were milled at 30 kV, using currents from 5 nA down to < 100 pA. The FIB-SEM carbon gas injection system was used to weld an Omniprobe microneedle to the wafer, and then the wafer to a TEM copper grid.

The wafers were analysed on a JEOL 2100 LaB_6 transmission electron microscope (TEM) with scanning-TEM (STEM) facilities and an Oxford Instruments system with Aztec EDX at UL. All TEM, STEM and EDX work was carried out using an accelerating voltage of 200 kV and beam current of ~110 μA.

2.3 SYNCHROTRON TECHNIQUES (DIAMOND LIGHT SOURCE)

The microfocus beamline I-18 at the Diamond Light Source, Didcot, Oxfordshire, UK was used to determine the oxidation state of the Fe in NWA 8114 by analysing the $1s \rightarrow 3d$ transitions and characteristic absorption edge energy in the Fe-K XANES spectra. The beamline has an energy range of 2.0-20.7 keV, and a minimum spot size resolution of ~2 × 2.5 μm, together with tuneable monochromators capable of resolving 0.1 eV spectra energy increments (Mosselmans et al., 2009).

2.3.1 Synchrotron X-ray Fluorescence (XRF)

XRF maps of the areas of interest were taken with a resolution of 2 × 2.5 μm primarily to locate the iron for Fe-K XAS analyses. XRF measures elements up to Zn in atomic weight to produce elemental maps using a beam between 8.5 and 10.0 keV. These maps were analysed using *PyMca 4.4.1* software.

2.3.2 Fe-K X-ray Absorption Spectroscopy (Fe-K XANES)

Fe-K X-ray Absorption Near Edge Spectroscopy XANES measurements were taken at 2 × 2.5 μm spot size. The spectra were taken over an energy range of 6900-7600 eV, with a high resolution of 0.1 eV over the region 7090-7145 eV, to accurately capture the $1s \rightarrow 3d$ pre-edge centroid and absorption edge positions. The data were processed and normalised through *Athena 0.9.24* software before analysing the $1s \rightarrow 3d$ pre-edge centroids by fitting a baseline and calculating the energy position of the centroid, using the methods of Hicks et al. (2014). The ferric-ferrous ratio (Fe^{3+} / Σ Fe) has been calculated using the silicate calibration scale (Hicks et al., 2014). In addition to point measurements, Fe-K XANES maps were made of two areas to show the variation in iron oxidation state visually over the absorption edge energy range 6900-7300 eV, with the Fe-K XANES spectra for each pixel being normalised and analysed using *MANTiS 2.06*.

Fe-K XANES were measured during four separate beamtime sessions in December 2014, July 2016, December 2016 and January 2018. Due to minor drift in the monochromators over time, an energy calibration is required to compare data from different sessions. An estimation of the energy variation was calculated by measuring reference materials such as Fe-metal foil, powdered magnetite, hematite and San Carlos olivine at each beamtime, determining their Fe-K $1s \rightarrow 3d$ pre-edge centroid and absorption edge positions, and adjusting all the results to the peak positions observed during the most recent beamtime (Hicks et al., 2017).

2.3.3 Transmission X-ray Diffraction (XRD)

The same I-18 beamline was used for transmission XRD measurements of a variety of clasts taken at 13 keV for between 60 and 300 s with a detector capable of imaging 2θ angles ranging between ~4° and ~40°. This corresponds to an observable *d*-spacing range of ~1.4 Å to ~13.7 Å. Measurements on a LaB_6 standard with *Dawn* 1.9 software (Basham et al., 2015) were used to calibrate the NWA 8114 data and obtain the *d*-spacings from the raw data. These were compared with measurements of other standards, magnetite, goethite, pyroxene, hematite etc and the ICDD database (ICDD, 2014) to identify the closest mineral match. Unit cell parameters were calculated after assigning *hkl* indices to the *d*-spacings and compared to unit cell parameters of mineral standards from the ICDD database (ICDD, 2014).

2.3.4 Fourier Transform Infrared Spectroscopy (FTIR)

Beamline B-22 at the Diamond Light Source was used to investigate sections A, B, C with reflectance FTIR, and section F with transmission FTIR (Cinque et al., 2011). B-22 has a spectral range of 10000 to 5 cm^{-1} and beam size of 3-15 μm at the sample, with achievable resolution of 0.07 cm^{-1}. Both point and map measurements were made using a 10 × 10 μm or 15 × 15 μm spot size and resolution of either 4 cm^{-1} (with 256 scans) or 8 cm^{-1} (with 128 scans), with a spectral range of 4000–500 cm^{-1}. *OPUS 7.0* (Bruker Optik GmbH 2011) software was used to process the data and a Krames-Kronig Transformation within it was used to obtain absorbance values from reflectance data.

2.4 ^{40}Ar-^{39}Ar dating

Four individual clasts were separated from NWA 8114 and subdivided into two fragments in order to investigate age and petrologic relationships. One fragment of each clast, with estimated masses of 0.5-0.7 mg, were neutron-irradiated for ^{40}Ar-^{39}Ar age determinations. The other fragment of each clast was mounted on carbon to characterise the mineralogy using SEM. The clast 3 fragment was subsequently made into a polished block for SEM-EDX analysis.

Samples were irradiated for 24 hr in position B2W of the SAFARI-1 reactor, Pelindaba, South Africa (irradiation MN2016a). Following irradiation, samples were placed in 3 mm diameter wells drilled into an aluminium disk and evacuated in a laser port attached to the noble gas extraction system at the University of Manchester, UK. Samples were baked at 150 °C overnight to reduce Ar blank levels. Samples were step heated using a 55 W CO_2 laser (Teledyne-Cetac Technologies Fusion 10.6 CO_2 laser system) using a 3 mm diameter beam having uniform energy distribution. Heating steps of 30 s duration were carried-out over the power interval 0.4 to 6 W using 5 to 11 steps until the sample fused. Noble gases were purified for 3 min using a Zr-Al getter (SEAES NP10) at 400 °C and then admitted to the mass spectrometer. Argon isotope measurements were determined using a Thermo Scientific Argus VI mass spectrometer equipped with 5 Faraday detectors. Data were corrected for blanks, mass discrimination, radioactive decay

and neutron interference reactions on K and Ca isotopes forming Ar isotopes. Procedural blanks were determined by carrying-out a sample analysis step without laser heating. The ^{40}Ar blank is equivalent to 2.68×10^{-12} cm^3 STP and was relatively stable during the course of the experiments, varying by <15%. The blank levels corresponds to between 8-50% (mostly <30%) of the ^{40}Ar released at each heating step and was monitored at regular intervals, usually after every third heating step. Instrument mass discrimination was established using aliquots of air with a ^{40}Ar/^{36}Ar = 298.6, and applying a linear mass fractionation correction. Air aliquots contained known volumes of Ar enabling instrument sensitivity to be determined and raw data to be converted to cm^3 STP. Neutron interferences were determined from high purity samples of calcium fluoride and potassium sulphate. Aliquots of Hb3gr hornblende (t = 1081.0 ± 2.4 Ma, 2σ; (Renne et al., 2011) were irradiated with the samples enabling the fluence parameters J and α to be determined by laser fusion of the hornblende standard (Table A1). We report the data uncorrected for martian (or terrestrial) trapped ^{40}Ar components, giving us approximate maximum ^{40}Ar/^{39}Ar ages to compare to other radiometric ages from the martian breccia in the literature.

3 RESULTS

3.1 Breccia and Clast Textures

NWA 8114 has a fresh distinctive black outer surface, a desert varnished relict of a fusion crust, with some visible feldspar and pyroxene clasts protruding (Fig. 1A) and a large spherule with concentric layers (Fig. 1B). However, minor terrestrial salt veins are apparent on the surface and in some of the polished sections. Some fracturing is seen, but no shock melt veins or maskelynite have been observed. The CT-scan in Fig. 1B shows a large spherule of diameter 1.5 mm with a central grain of ~0.6 mm and multiple further concentric layers including a fine-grained outer rim, similar to a spherule described by Wittmann et al. (2015) and another spherule described by Hewins et al. (2017).

NWA 8114 has similar textural and mineralogical features to those described in NWA 7034 (Agee et al., 2013; Santos et al., 2015), NWA 7533 (Humayun et al., 2013; Hewins et al., 2017) and NWA 7475 (Wittmann et al., 2015). In section, the sample has a clastic, brecciated texture comprised of clasts of feldspar grains (26%), pyroxene (18%), Fe-Ti oxides (6%), small amounts of Cl-apatite as well as some melt rock, all bound by a dark, fine grained matrix (50%). The SEM images of the sections (Fig. 2A, Fig. 3) show the range of clast size (5 μm to a few mm), and clast shape (from angular to rounded) bound in the fine grained (<5 μm) crystalline matrix. The pyroxenes are the main focus of our study, but we also identified alkali feldspar clasts with cryptoperthite textures (Fig. 4H) indicating slow cooling for them at sub-solidus temperatures. An iron oxide intergrowth has a Ti-rich centre (Fig. 4C) and some iron oxide clasts contain

pyrite inclusions (Fig. 4I), similar to those studied by Lorand et al. (2015), who found Fe-oxides to be terrestrial weathering products of martian pyrites.

Many of the pyroxene clasts exhibit exsolution lamellae on the (001) lattice planes, including both augite lamellae in clasts which are mainly pigeonite pyroxene (Fig. 4D and F), and pigeonite lamellae in bulk augite clasts (Fig. 4E, Fig. 5). Some pyroxene clasts, including low-Ca pigeonite and augite, contain small crystals (<2 μm) of iron oxide (Fig. 4A,B,D-G, Fig. 6, Fig. 7A), like those examined by Leroux et al. (2016).

Some relict pyroxene fragments show strikingly high porosity of up to ~5% (Fig. 4A,B,G, Fig. 7A). These have plagioclase-rich rims (Fig. 4A,B,G) similar to clump-aureole structures (Hewins et al., 2017). The relict pyroxene with feldspar aureole (Fig. 4B) resembles dustball-like aggregates described by Hewins et al. (2017, Fig.S2d). The pyroxene clasts have been investigated further with STEM, XAS and XRD (Section 3.4).

Some angular clasts have fine-grained rims and feldspar veining as well. Some clasts show signs of limited melting taking place after the clast formed. One example of this is shown by the large relict pyroxene clast with iron oxide grains crosscut by feldspathic veins (Fig. 2, Fig. 6). In a region spanning ~20 μm either side of each vein there are fewer iron oxide grains and backscattered electron images show devitrification and resultant microcrystalline axialites (Fig. 6B). In the same clast, the feldspar veins are truncated by a rim with accreted grains of up to 100 μm. This rim contains the ends of the veins and feldspar, giving evidence of melting with subsequent devitrification (Fig. 2C).

One clast consists of a 600 μm iron oxide grain (Fig. 7B) that is partially surrounded by terrestrial calcium carbonate veins. It also contains inclusions of pyrite and FeTi oxide. In section 3.5 we demonstrate that this clast is composed of goethite.

3.2 Mineral Compositions

NWA 8114 relict pyroxene clasts without exsolution lamellae include low-Ca pyroxene and pigeonite (Fig. 4B and G, Fig. 8) $En_{44-72}Fs_{26-50}Wo_{2-6}$, and augite (Fig. 4A, Fig. 8) $En_{31-53}Fs_{19-24}Wo_{28-45}$. Compositions of pyroxene clasts with exsolution lamellae are plotted in Fig. 8 and are similar to the ranges seen in the pyroxene clasts without exsolution lamellae. These include bulk pigeonite $En_{44}Fs_{50}Wo_{6}$ with augite $En_{37}Fs_{26}Wo_{37}$ exsolution lamellae (Fig. 4D), bulk augite $En_{31}Fs_{24}Wo_{45}$ with pigeonite $En_{36}Fs_{47}Wo_{17}$ exsolution lamellae (Fig. 4E) and bulk pigeonite $En_{52}Fs_{43}Wo_{5}$ with augite $En_{42}Fs_{18}Wo_{40}$ exsolution lamellae (Fig. 4F), although as the lamellae are only 1-2 μm wide the lamellae compositions may include some of the bulk clast.

The large relict pyroxene clast with a fine grained rim (Fig. 2A, Fig. 6) was found to be predominantly relict pigeonite with SEM-EDX composition $En_{30-33}Fs_{49-59}Wo_{11-18}$ with submicron grains of iron oxide and some likely fine submicron feldspar grains given the spectra show Al_2O_3

at 6.4% and traces of Na_2O 0.7%, and K_2O 2.5% (Table 2, Fig. 6A3). The veins cross-cutting it contained mainly plagioclase $An_{29}Ab_{64}Or_7$ (with a range of $An_{20-39}Ab_{60-72}Or_{0-19}$) though also small amounts of orthoclase $An_0Ab_{13}Or_{87}$ and hyalophane of $An_{12}Ab_{30}Or_{52}Cn_6$ were found, similar to veins seen in a spherule in paired stone NWA 7533 (Hewins et al., 2017, Fig 6B). The ~20 μm melt areas each side of the veins were found to be composed of stoichiometric pyroxene $En_{37}Fs_{42}Wo_{21}$ in the light crystallites (Table 2, Fig. 6A5), while the dark areas in BSE SEM images (Fig. 6A6) were non stoichiometric (Table 2) and relatively enriched in Al, Na and depleted in Fe, Mg and Ca compared to the light crystallites, likely feldspathic, but the SEM spot size was too large to capture just stoichiometric feldspar and still included pyroxene.

The feldspar clasts compositions are $An_{12-46}Ab_{50-82}Or_{0-25}$ and alkali feldspar clasts show cryptoperthite texture with a range of $An_{0-10}Ab_{8-95}Or_{3-92}$ or $An_{1-5}Ab_{11-86}Or_{11-88}$ (Fig. 4H, Fig. 9). The compositional range of plagioclase-rich rims on pyroxene clasts is andesine, $An_{30-55}Ab_{43-66}Or_{2-5}$ (Fig. 4A,B,G, Fig. 9), which closely matches the range of plagioclase seen in the veins cutting the spherule (Fig. 2B).

The EPMA map of the relict pyroxene clast with a plagioclase aureole (Fig. 7C) shows the areas with more plagioclase grains (blue = Al) ($An_{18-40}Ab_{51-65}Or_{2-22}$) versus those with more pyroxene grains (dark green = Ca with Fe) ($En_{41-48}Fs_{17-29}Wo_{26-39}$). Two measurements of the Fe oxide grain marked 'gt' (Fig. 7B) showed a total oxide weight of 77.3% and 78.1% (Fe was calculated as Fe^{2+}, (Table 2), indicating that it contains Fe^{3+} and/or a hydrated phase. This matches EPMA analyses for goethite in other planetary materials e.g. 75.7% (Zhu et al., 2012) and goethite measured as 86.5% Fe_2O_3 (equivalent to 77.8% FeO) (RRUFF Database, 2006). Both measurements also included 0.9 wt% NiO, which was rarely above 0.1 wt% in other measurements taken across different clasts (predominantly pyroxene and feldspar) in NWA 8114. The goethite grain contains small amounts of Si, Al, Ti, S and P, consistent with possible titanomagnetite and pyrite and other precursor material. The goethite is likely a pseudomorph after euhedral pyrite, inheriting the Ni, similar in shape to pyrite and iron oxides seen in paired stones (Wittmann et al., 2015; Lorand et al., 2015; Hewins et al., 2017).

Other iron oxide grains in NWA 8114 include a Ti-rich magnetite intergrowth (Fig. 4C). Pyrite is present in very small quantities and usually within iron oxide clasts. Non-stoichiometric sulfide is also present, and this may be related to alteration. One large grain of Cl-apatite (240 × 100 μm) was observed (Fig. 3: bright green), otherwise Cl-apatite is present as <50 μm grains, or dispersed in the matrix.

3.2.1. Mineralogy of separated clasts for Ar- Ar

Four clasts that were less than one mm each in diameter were separated from our NWA 8114 stone. Half of each clast was dated using ^{40}Ar-^{39}Ar (see section 3.7). Two clasts were highly zoned plagioclase: Clast 1: $An_{19-41}Ab_{53-73}Or_{5-8}$, Clast 2: $An_{47-51}Ab_{40-50}Or_{0-9}$. Clast 3 is an augitic pyroxene clast $En_{24-39}Fs_{13-26}Wo_{48-50}$ with up to 8% plagioclase inclusions $An_{12-55}Ab_{45-74}Or_{0-18}$ and

a marginal band of terrestrial calcite (Fig. 9, Fig. 10A, Table 2). The pyroxene shows porosity of at least 3% throughout, together with small iron oxide grains, similar to relict pyroxene clasts with feldspar aureole seen in the polished sections (Fig. 4A,B,G, Fig. 7A). Iron oxides, Ti-magnetite and Cl-apatite inclusions were also present in clast 3. Clast 4 is a feldspar-rich clast.

3.3 TEM Investigations of Pyroxene Texture

We analysed a total of 7 TEM extracted wafers of NWA 8114 relict pyroxenes and their breakdown products. Two FIB-TEM extractions were taken from the relict pigeonite clast (Fig. 2A) containing iron oxide grains (FIB1 and FIB3, Fig. 11, Fig. 12). TEM-EDX revealed a porphyritic, submicron mixture of a K-bearing feldspathic, glassy material, iron oxide (~10-20%), with the remainder being discrete pyroxene laths up to 500 x 200 nm in size (Fig. 12C,D,E). A FIB-TEM extraction from a low-Ca $En_{72}Fs_{26}Wo_2$ relict pyroxene with feldspar aureole (Fig. 4B, Fig. 11B FIB7) showed the granoblastic texture, with many grain boundaries near 120°, evidence for re-crystallisation of the pyroxene. This clast had porosity of up to ~5%.

Table 3 gives TEM-EDX data for pyroxene from FIB1 and FIB3, with compositions ranging $En_{32-57}Fs_{21-51}Wo_{13-38}$, including both pigeonite and augite. The broader beam size EPMA data suggests an Fe-rich bulk pyroxene, whereas the finer scale TEM-EDX resolution mostly indicates a lower Fs content in discrete pyroxene. This break down was also seen in another low-Ca relict pyroxene with feldspar aureole, $En_{65-68}Fs_{29-33}Wo_2$ (Fig. 4G). Iron oxide grains were present in the pyroxene but no aluminium silicate was observed. The apparent difference in Fs contents of pyroxene between EPMA and TEM-EDX analyses is likely due to submicron iron oxide grains being included in the EPMA point analyses.

Iron oxide grains were also found in an augite-dominated relict pyroxene with feldspar aureole, $En_{53}Fs_{19}Wo_{28}$ (Table 3, FIB6A, 6B, Fig. 4A), but no aluminium silicate was seen in this sample, likely due to TEM-EDX analyses measuring more than one phase. Further TEM-EDX data showed an intermediate composition with enrichment in SiO_2 57.4 wt% and Al_2O_3 4.6 wt%, and lower FeO 3.7 wt% compared to stoichiometric pyroxene (53.4 wt% SiO_2, 4.1 wt% Al_2O_3, 6.4 wt% FeO). This suggests that some of the Fe in the pyroxene has been oxidised, resulting in the formation of separate magnetite grains and a mixture of pyroxene and a K-bearing feldspathic glassy material.

3.4 Iron Oxidation State

To investigate the oxidation state of the iron, XRF and Fe-K XANES maps (Fig. 13) were taken across the relict pigeonite clast (Fig. 2A, white box), where TEM showed the pyroxene breakdown occurring (Section 3.3), and the relict pyroxene with feldspar aureole (Fig. 7A, white box), which had similar small magnetite grains within the pyroxene and plagioclase. Fe-K XANES point measurements were taken on other similar relict pyroxene clasts with small iron oxide grains and porosity: the low-Ca relict pyroxene with feldspar aureole from which FIB2

was extracted (Fig. 4G), a high-Ca relict pyroxene with feldspar aureole, from which FIB6A was extracted (Fig. 4A), and part of the augite pyroxene clast that also underwent ^{40}Ar-^{39}Ar dating (Fig. 10).

Fig. 13 G and H show the normalized intensity across a range of energy values corresponding to the Fe-K absorption edge, the near-vertical line on the graph, where the 1*s* electron of Fe absorbs an X-ray photon. The small peak before the absorption edge energy corresponds to the pre-edge $1s \rightarrow 3d$, known as the pre-edge centroid. If the iron is more oxidized, then the pre-edge centroid and absorption edge shift to slightly higher energy values. Values for these are given in Table 4 and plotted in Fig. 14.

The pyroxene analyses indicate oxidation, as the pre-edge centroid and absorption edge are both noticeably higher when compared with unaltered monomineralic pyroxene clasts (Fig. 13G, Fig. 14, Table 4). Using the calibration scale of Hicks et al. (2014), the relict pigeonite clast, relict pyroxene with feldspar aureole, augitic and low-Ca relict pyroxenes with feldspar aureole have $Fe^{3+}/Fe_{tot} \leq 25\%$. Fe-K XANES measurements for unaltered monomineralic pyroxene clasts show negligible ferric iron content (Fig. 13G, Fig. 14).

Two Fe-K XANES measurements on the Fe oxide grain (Fig. 10D) closely match the goethite standard analysis (Fig. 13H), with the $1s \rightarrow 3d$ pre-edge centroid 0.33 and 0.44 eV lower than the standard and the Fe-K absorption edge energy 0.40 eV higher than the standard (Table 4). The XRF map of this goethite grain (Fig. 7D) shows the presence of Ni throughout the grain, consistent with the EPMA measurement recording 0.9% NiO, higher than NiO recorded anywhere else in these samples. High NiO was previously seen in pyrite (Lorand et al., 2015), but no clasts of pyrite were observed in our three sections studied here (though pyrite clasts have been found in a fourth polished block of NWA 8114).

3.5 Mineral Identification by XRD

XRD measurements were taken across the full range of clasts and used in particular to distinguish between different iron oxides and hydroxides. Grains in the relict pyroxene with feldspar aureole marked 'X' (Fig. 7A) gave *d*-spacing peaks that matched the XRD measurement of a powdered magnetite standard (X1-X4, Fig. 15A, Table 5). These peaks were used to calculate unit cell dimensions, giving a calculated cubic cell parameter in two grains of 8.389 ± 0.003 Å and 8.391 ± 0.002 Å compared with magnetite standards 8.375-8.405 Å (ICDD, 2014). A measurement in the low-Ca relict pyroxene with feldspar aureole (C29, Fig. 15C) also gave the cubic cell parameter as 8.390 ± 0.01 Å (Table 5). This shows that the sub-micron iron oxide grains in two of the clasts showing this texture are magnetite.

The *d*-spacing peaks for the 'gt' grain in Fig. 7B indicate a good match with the goethite FeO(OH) standard, as seen by two typical measurements (Fig. 15B) taken from the fifty measurements of the XRD map across the clast (Fig. 7D). The second typical measurement C5-

32 also shows *d*-spacings consistent with magnetite and/or maghemite (Table 5), confirming they co-exist with the goethite. The *d*-spacings were used to calculate unit cell dimensions (Table 5) together with further such calculated unit cell dimensions from the XRD map. These are plotted in Fig. 15B, showing a close fit against a population of goethite data (ICDD, 2014).

Measurements from a further three pyroxene clasts and one plagioclase and one K-feldspar clast are also shown in Fig. 15C. It can be seen that the pyroxene clasts often have peaks matching the magnetite standard, suggesting that where iron oxide grains are seen in pyroxene, these are usually magnetite.

3.6 FTIR Search for Evidence of Hydration

FTIR reflectance data showed an absence of any hydration in the relict pigeonite clast described previously with TEM (Fig. 16) or across the rest of the relict pyroxene with feldspar aureole containing magnetite (Fig. 7A). FTIR reflectance data (Fig. 16) taken over the goethite grain marked gt (Fig. 7B) indicates a consistent absorption peak at 3145 cm^{-1} matching the synthetic goethite in Beck et al. (2015), and absorption peaks at 895 cm^{-1} and 795 cm^{-1} (Gotić and Musić, 2007), distinguishing it from other hydrated iron oxides.

3.7 ^{40}Ar-^{39}Ar dating

Apparent age and Ca/K spectra are displayed for three alkali feldspar clasts (clasts 1, 2 and 4) and one predominantly augite clast (clast 3, Fig. 10) in Fig. 17 and the data are given in Table A1. Data for all samples show considerable scatter on $^{39}Ar/^{40}Ar$-$^{36}Ar/^{40}Ar$ correlation diagrams (not shown), therefore it is not possible to establish if the sample contains trapped terrestrial or martian Ar components. Correction for assumed trapped terrestrial atmosphere results in a larger correction at low temperature, but relatively minor at higher temperatures. Due to the uncertainty in the trapped Ar composition, any ^{40}Ar excesses, and given that a proportion of the ^{36}Ar may have been formed by cosmic-ray interaction during transit of the parent meteoroid, the apparent ages shown in Fig. 17A represent maximum approximate age values. Precise ages and errors were not obtained due to the disturbed nature of the gas release patterns for the separated clasts.

The augite clast 3 shows a relatively flat spectrum (Fig. 17A) with apparent ages varying between 925 to 1293 Ma but with most spanning the interval 1100 to 1250 Ma. The high temperature step ages of 1130 Ma to 1250 Ma are regarded as more reliable, as there is a plateau in the gas release and Ca/K ratios. It is this approximate age range that we use to compare to other radiometric ages from the martian breccia (Fig. 18). The Ca/K spectrum of the augite (Fig. 17B) is reasonably stable for the initial 50% ^{39}Ar release with a value of a ~50, and then rises steeply to a maximum of ~700. This variation is considered to reflect the difference between the higher Ca in the augite, the lower Ca and higher K in the feldspar inclusions and higher Ca in the calcite vein in the clast (Fig. 10). EPMA data for comparable clasts confirms up to 2000 ppm of K in plagioclase and usually less than 200 ppm K in pyroxene, which suggests the 546 ppm K

(Table A1) is predominantly pyroxene but with feldspar impurities. As calcite does not contain K, we do not expect it to affect the ages.

The spectra for the feldspar clasts (Fig. 17) rise from a calculated ~500 Ma (clast 1 and 2) to maxima of 2620 Ma and 2640 Ma in clasts 1 and 4, but higher at 3440 Ma in clast 2. Staircase age spectra might indicate samples that have experienced diffusive loss of ^{40}Ar during thermal pulses or shock events. The K/Ca spectra for the feldspar have some variation throughout the releases (Fig. 17B) with the majority of steps having values between 28 and 31 (mol/mol). We regard the data for the feldspar clasts as too imprecise to report any reliable ages resulting from shock resetting etc.

4 DISCUSSION

Based on our mineralogical and Ar-Ar studies, we have identified five distinct events in the history of the NWA 8114 parent breccia, ordered here from earliest to last. Stages 2-4 are considered to have occurred in quick succession as a result of the impact event that formed the breccia. We discuss our results in the context of impact crater ejecta blankets and the thermal structure of the regolith on Mars, and provide a simple Fourier cooling model constrained by our mineralogical data.

4.1 Five Distinct Events in the Martian Breccia's Formation

4.1.1 Stage 1: Original magmatic crystallisation

The compositions of the pigeonite host pyroxenes and their augite exsolution lamellae for six exsolution-bearing clasts suggest that these originally crystallised from a magmatic event with subsequent subsolidus cooling recorded between 900 °C to 1050 °C (Fig. 8, Lindsley and Andersen, 1983). The lamellae are the result of slow cooling from the original magmatic event(s). As the exsolution lamellae vary in width and distance of separation (Fig. 4D,E,F), these pyroxenes likely cooled at different depths and may have originated from different parent rocks. This was also noted by Leroux et al. (2016) who measured the lamellae in a TEM study of three augite clasts bearing pigeonite lamellae, and one pigeonite clast containing augite exsolution lamellae in paired stone NWA 7533. The Ti-magnetite, Cl-apatite, plagioclase and alkaline feldspar are also magmatic precursor material, likely originating from more than one magmatic event as trends in pyroxene REE chemistry and Mg# suggest that the igneous clasts cannot be related by fractional crystallisation (Santos et al., 2015). Cryptoperthite feldspar also indicates a slow-cooling magmatic history (Fig. 4H). ^{147}Sm-^{143}Nd dating of whole rock and mineral separates suggest that these magmatic precursors and impact melt rocks probably formed ~4.44 Ga ago (Nyquist et al., 2016).

4.1.2 Stage 2: Formation of accretionary lapilli and formation of the breccia

The spherule with diameter 1.5 mm seen with the CT scan shows distinct layers of different compositions (Fig. 1B), comparable to accretionary lapilli from other planetary materials. Accretionary lapilli are found throughout Earth's stratigraphic record at large impact sites on the Earth; at the 1850 Ma (Krogh et al., 1982) Sudbury impact basin, (Huber and Koeberl, 2017), the 65 Ma (indicated by the K/T boundary), ~195 km diameter, multi-ring Chicxulub crater (Gulick et al., 2008; Yancey and Guillemette, 2008), and the 14.8 Ma (Schmieder et al., 2018), ~26 km diameter, Ries crater (Graup, 1981; Siegert et al., 2017). They are also present in the Apollo lunar samples, formed in impact events (Mckay and Morrison, 1971). They appear similar to pyroclastic accretionary lapilli, that start to form in the hot volcanic plume where water vapour facilitates the accretion of dust into pellets, which fall out into a pyroclastic density current (Gilbert and Lane, 1994; Schumacher and Schmincke, 1995). The pellets circulate in the upper turbulent flow where concentric dust layers accrete as they harden, and these accretionary lapilli tend to be found in the upper layers of the current deposit, ignimbrites, with pellet and ash fallout layers occurring afterwards (Brown et al., 2010; Branney and Brown, 2011).

Molten silicate, or any condensable material in the ejecta curtain could be the binding agent for impact-derived accretionary lapilli (Johnson and Melosh, 2014), as higher temperatures are reached compared to volcanic plumes that consist mainly of hot gas and solid ash particles. This would explain how they can form on the Moon and Mars without there being much atmosphere or large volumes of water vapour present.

Wittmann et al. (2015) suggested the accretionary dust rims seen in the martian breccia may have formed due to sintering in a hot ejecta plume, though they also drew parallels with accretionary lapilli in terrestrial suevites thought to have formed under base surge conditions. A base surge formation mechanisms would also explain the presence of impact melt rock clasts. Fluidized ejecta patterns are observed at craters on Mars and base-surge deposits on the Moon show radial flow patterns (Mckay and Morrison, 1971), providing further evidence that depositional processes via density currents may occur around large impacts, even if the mechanism for them is not currently understood. By this scenario, accretion of the breccia followed immediately after the presence of the envisaged density flow current.

4.1.3 Stage 3: The breakdown of pyroxene under high temperature, oxidising conditions.

Immediately after the impact, the regolith breccia was assembled and compacted in a thick, hot ejecta blanket, likely experiencing sustained high temperatures, of at least 700 °C based on the oxidation studies described later in this section, from the impact event for some weeks or months. Our TEM data shows that the large relict pigeonite clast with iron oxide grains $Wo_{12-18}En_{31-34}Fs_{47-56}$ (Fig. 12) has partially melted and partially devitrified to form magnetite and K-bearing feldspathic glassy material at a submicron scale (Fig. 12B-E). The iron oxide is assumed to be magnetite as a pyroxene clast with similar grains was shown to be magnetite with XRD

(Fig. 15, Table 5). The pyroxene breakdown was associated with oxidation, as shown by the Fe-K XANES data (Table 4), which indicate up to 25% Fe^{3+}/Fe_{tot} (Hicks et al., 2014) compared to no oxidation seen in unaltered monomineralic pyroxene clasts (Table 4). FTIR suggests this alteration assemblage is anhydrous (Fig. 16). However, although now anhydrous, we note that the original oxidative breakdown and formation of accretionary clasts may have involved the action of water vapour. This water vapour would have been driven off during cooling from high temperature in the porous regolith. Many pyroxene clasts in NWA 8114, from low-Ca to high-Ca pyroxene, show submicron magnetite grains within them (Table 3, Fig. 11). TEM-EDX results for these also show an intermediate, non-stoichiometric composition enriched in SiO_2 and Al_2O_3 and depleted in FeO compared to pyroxene, indicating that some of the Fe from the pyroxene has been oxidised, forming the separate magnetite grains (Table 3, Fig. 11). Not all pyroxenes show this breakdown. However, it is seen in some examples of augite, pigeonite and orthopyroxenes so the breakdown occurrence does not depend upon exact pyroxene composition.

Some iron oxide grains have also been observed in those clasts formed of pyroxene with exsolution lamellae. These iron oxide grains tend to be larger, over a micron in size, and are often present along cracks (Fig. 4D,F). They are not aligned or associated with the exsolution lamellae from original crystallisation, suggesting they formed later. As Leroux et al. (2016) noted, trails of magnetite and silica inclusions resemble fluid inclusion trails.

Oxidation of planetary pyroxene has been associated with shock effects in previous studies of meteorites. The breakdown of both Ca-rich and Ca-poor pyroxene to iron oxide that we have observed in NWA 8114, and also seen in pyroxenes in paired stone NWA 7533 (Leroux et al., 2016; Hewins et al., 2017), has some analogies with the breakdown of pyroxene in ureilites by impact smelting. In ureilites, it has been suggested ~50% of the pigeonite has been reduced by impact smelting and contains a fine distribution of Fe-metal, and diverse felsic glasses containing SiO_2 and Al_2O_3 (Warren and Rubin, 2010). The impact event(s) on Mars took place under much more oxidising conditions, calculated from magnetite-ilmenite pairs to be FMQ + 2 to FMQ + 4 log units (Santos et al., 2015). Thus, we see iron oxide grains (rather than Fe-metal) and a K-bearing feldspathic glassy material. Furthermore, the impact shock of the breccia was lower than that of ureilites, with the former's maximum shock pressure estimated at 5-15 GPa from pyroxene and feldspar fractures, occasional shock melt veins (Wittmann et al., 2015), and the absence of any maskelynite (Santos et al., 2015).

An appropriate, simplified pyroxene oxidation reaction adapted from Leroux et al. (2016) is:

$$6\ MgFeSi_2O_6 + O_2 = 6\ MgSiO_3 + 2\ Fe_3O_4 + 6\ SiO_2 \qquad \text{Equation 1}$$

In reality, some of the Fe remains as FeO in the pyroxene so pure enstatite is not predicted from this reaction.

The altered pyroxene in LAR 04315 ureilite is unusually porous, with pre-terrestrial porosity estimated to be 9-12% (Warren and Rubin, 2010). The porosity is thought to have been caused by the impact smelting, as the pyroxene still shows near optical continuity after smelting, suggesting it was coherent beforehand. We see similar porosity (Fig. 4A,B,G, Fig. 7A) of up to 5% in the breccia clasts showing pyroxene breakdown, and this porosity is also observed in the augitic clast 3 that was dated to provide approximate maximum ages using ^{40}Ar-^{39}Ar (Fig. 10).

In another approach to shock effects in pyroxene minerals, McCanta and Dyar (2017) used experimental shock analyses (21-59 GPa) of pyroxene to show the Fe^{3+} increased ×2-6, even without free oxygen, overprinting the original magmatic fO_2 values. Mössbauer data showed this increase was within the pyroxene structure itself; BSE and TEM imaging showed no new phases. The mechanism of incorporating H^+ ions in the crystal structure is suggested, as hydrogen diffusivity increases as total Fe content increases and nearly all natural clinopyroxene contains ppm levels of H (McCanta and Dyar, 2017). The redox exchange reaction (McCanta and Dyar, 2017) proposed by Mackwell and Kohlstedt (1990) incorporating hydrogen is:

$$H^{+}_{px} + Fe^{2+}_{px} \longleftrightarrow \tfrac{1}{2}\,[H_2]_{gas} + Fe^{3+}_{px} \qquad \text{Equation 2}$$

This mechanism provides some insight to the overall link to shock processes causing oxidation, however, in NWA 8114 the oxidation in pigeonite is associated with the formation of submicron-sized magnetite grains, rather than the oxidation being incorporated into the pyroxene structure. An oxidising agent is required, assuming the original pyroxene before breakdown and relict pyroxene afterwards have a similar level of oxidation, in order for the magnetite to form. Equation 2 offers one possible mechanism. Alternatively, transient water may have been present at the time of the impact event, perhaps from melting subsurface ice in the regolith, to cause the oxidation and breakdown of pyroxene observed. This would be consistent with the formation of accretionary rims around clasts e.g. (Gilbert and Lane, 1994) within the martian breccia.

Studies have also explored the oxidation of iron within the silicate matrix of pyroxenes, at a variety of temperatures (400-1000 °C) and for different durations up to 28 days (Straub et al., 1991). Mossbauer reflectance spectra confirmed that the proportion of Fe^{3+} ions in oxidised pyroxene increases at higher temperatures and after longer heating time periods. Nanophase hematite formed in both enstatite oxidised at 700 °C for 28 days and pigeonite oxidised at 1000 °C for 14 days. However, oxidation of augite at 700 °C for 28 days and 800 °C for 3 days showed structural Fe^{3+} ions were present in the pyroxene structure, rather than nanophase hematite.

Similarly, an analogue martian sample was oxidised in air at 700 °C for 1, 3 or 7 days (Minitti et al., 2002). This was a calculated melt sample composition representative of the SNC meteorites, low in Al_2O_3 (~8.0 wt%) and high in total FeO (~19 wt%) relative to terrestrial basaltic melts (Johnson et al., 1991), prepared for a range of different crystallinities (0–80 % crystalline).

Electron and spectral microscopy showed nanophase hematite as the dominant oxidation product in pigeonite, while the behaviour of the 1.0 and 2.3 μm visible and near-infrared (VISNIR) absorptions for augite were consistent with the development of Fe^{3+} (Minitti et al., 2002).

Both of these studies show the production of submicron iron oxide grains in pigeonite at high temperatures, similar to that observed in NWA 8114 suggesting it also experienced a high temperature oxidation process, likely due to heat from an impact event. Both show that oxidised augite tends to retain the Fe^{3+} within its structure.

Olivine in some martian shergottites has been shown to contain iron metal nanoparticles, which are responsible for heterogeneously darkening the olivine to brown as a result of shock (Takenouchi et al., 2017). It is thought that the disproportionation reaction of olivine ($3Fe^{2+}_{olivine} \rightarrow Fe^{0}_{metal} + 2Fe^{3+}_{olivine} + V_{olivine}$ where $v_{olivine}$ is a vacancy in olivine) is responsible for this, requiring temperatures over 1500 K, pressures over 30 GPa and a shock duration of at least ~90 ms (Takenouchi et al., 2017). These pressures are higher than those experienced by NWA 8114 but similarly show shock-induced oxidation in some martian shergottites.

Our results show the decomposition and oxidation of pyroxene in NWA 8114, similar to paired meteorite NWA 7533 (Leroux et al., 2016). By comparison to the studies above, we identify it to be the result of shock oxidation and heating. Leroux et al. (2016) suggested this reaction occurred ~1000 °C and only affected some of the pyroxenes, so concluded it was a separate high temperature event to that which formed the breccia. We suggest the oxidation could take place at ~700+ °C and thus is likely to be the same impact event that resulted in the formation of the breccia and accretionary rims around some of the clasts. The ^{40}Ar-^{39}Ar potential maximum age range for the predominantly augitic pyroxene clast 3 (Fig. 10, Fig. 17) that shows porosity and iron oxide grains similar to the pyroxene breakdown texture described above in the polished sections, indicates the high temperature shock event was approximately 1.13 Ga to 1.25 Ga.

Comparing with other available data (Fig. 18), this is in good agreement with ten whole rock ^{40}Ar-^{39}Ar ages of 1.159 to 1.407 Ga in pair NWA 11522 (Cassata et al., 2018). It is also consistent with two of the three U-Th-total Pb ages of monazite in apatite reported as 1.0 ± 0.4 Ga, 1.1 ± 0.5 Ga and 2.8 ± 0.7 Ga, and interpreted to have been formed by hydrothermal alteration (Liu et al., 2016). K-Ar whole rock ages of ~1.56 Ga (Cartwright et al., 2014) are in reasonable agreement with our augite age, given that the K-Ar age is a bulk measurement.

^{40}Ar-^{39}Ar plateau ages of 1.411 ± 0.009 Ga for a plagioclase sample, 1.361 ± 0.003 Ga for an alkali feldspar sample together with 0.798 ± 0.052 Ga for another alkali feldspar sample for paired stone NWA 7533 are reported by (Lindsay et al., 2014), Further work for NWA 7034 feldspars shows ^{40}Ar-^{39}Ar plateau ages from 1.4 to 2.3 Ga, noting 1.285 ± 0.004 Ga for a bulk sample of 202 μg and suggests the bulk sample age is a result of averaging the three age groups observed in the separated feldspar samples: >2.0 Ga, 1.4 to 1.6 Ga and 0.8 Ga (Lindsay et al., 2016).

Cl-apatite U-Pb ages of 1.35-1.5 Ga (Yin et al., 2014; Bellucci et al., 2015; McCubbin et al., 2016) and zircon U-Pb young ages of ~1.4-1.7 Ga (Humayun et al., 2013; Yin et al., 2014; Nemchin et al., 2014; Bellucci et al., 2015; McCubbin et al., 2016) show some variation. These different isotopic dating methods have higher closure temperatures than the Ar system, which could - taken at face value - suggest the 100 Ma to 300 Ma difference is an indication that the Ar-isotope system stayed open for a longer time. However, we note that with the uncertainties in the excess Ar corrections, those values are indistinguishable from the ~1.1 to 1.4 Ga ages discussed above (Lindsay et al., 2014; Lindsay et al., 2016; Cassata et al., 2018) considering the analytical error, and 1.13 Ga to 1.25 Ga may date the main high temperature event within the regolith, immediately after the main impact event associated with the breccia.

4.1.4 Stage 4: The formation of feldspathic veins

Textural evidence shows that the feldspar veins crosscut and postdate the impact oxidised relict pigeonite clast (Fig. 2, Fig. 6). The presence of a 20 μm region each side of each vein with recrystallised grains of pigeonite among dendrites enriched in Na and Al, likely submicron plagioclase (Fig. 6) suggests a possibility that the temperature at which the veins were emplaced caused some melting and recrystallization in the oxidised relict pigeonite clast. Some of the clast's accretionary rim shows signs of melting and feldspar migration (Fig. 2).

However, orthoclase-rich veins on Earth often occur as a result of hydrothermal alteration below 500 °C (McSwiggen et al., 1994; Deer et al., 2001), which is suggested as a mechanism for the formation of similar veins seen in NWA 7533 (Hewins et al., 2017). Hewins et al. (2017) also described hyalophane veins. Hyalophane contains 5-65% celsian, and terrestrial examples include hyalophane-zoisite veins in shales near Litosice, Czech Republic (Zak, 1991) and Ba-bearing alkali feldspars, hyalophane $An_{0.3}Ab_{8.2}Or_{25.8}Cn_{65.7}$ and celsian in the green mica schists of Hemlo-Heron Bay in Ontario (Pan and Fleet, 1991), both being a result of hydrothermal alteration. In our study we have identified a small amount of hyalophane $An_{12}Ab_{30}Or_{52}Cn_{6}$ in NWA 8114 veins, but there is little clear mineralogical evidence of other hydrothermal assemblages or alteration in the meteorite. If the temperature did not go above ~400°C it is hard to explain the recrystallized grains in the ~20 μm area bordering the veins, but the nature of the veins and terrestrial analogues do leave open the alternative possibility of a hydrothermal origin.

To explain the feldspar veins in the breccia clasts, we envisage that the impact event may have aggregated the breccia in a thick, hot insulated ejecta blanket, where high enough temperatures were maintained to remobilise and melt feldspar rich domains (Fig. 6). The diopside-anorthite-albite ternary eutectic lies at ~1150 °C, though temperatures are unlikely to have reached this given some zircons did not reset (~ 1000 °C) and pyroxene exsolution lamellae are preserved (~ 900 °C). Impurities and other components would lower the eutectic, and the liquidus temperature for a monzonite could be as low as 800 °C, which is in agreement with a textural study of the degree of melting in the submicron matrix (McCubbin et al., 2016).

The andesine-rich $An_{29}Ab_{64}Or_{7}$ veins that crosscut the relict pigeonite clast and the Na and Al enrichment in the dendritic texture bordering the veins, are evidence of *in situ* melting, of a feldspar-rich domain. Similar andesine is also seen in the fine grained rim of this clast, sometimes with a melted texture in the adjacent pyroxene. The range of feldspar in the veins is also similar to feldspar $An_{33.8}Ab_{62.6}Or_{3.6}$ observed in veins by Hewins et al. (2017).

Other pyroxene clasts with crystalline andesine rims $An_{25\text{-}55}Ab_{43\text{-}75}Or_{2\text{-}5}$ (Fig. 4A,B,G) rather than accretionary rims, closely match the $An_{32\text{-}56}$ rims of 'oval somewhat spherulite-like clump-aureole structures' by Hewins et al. (2017). Clasts in Fig. 4A,B,G also show concave margins in pyroxene which indicate vesicle walls, consistent with vesiculated melts (Hewins et al., 2017). These authors suggested formation as spherulitic growth on remnants of pyroxene or hydrated dust pellets.

The evidence of high temperatures – either melting or possibly hydrothermal action - we have identified is further evidence to the previously described pyroxene breakdown textures, that shortly after formation, the breccia was maintained at high temperatures.

4.1.5 Stage 5: Low temperature aqueous alteration and goethite formation

The presence of goethite FeO(OH) within the relict pyroxene with feldspar aureole as shown by the XRD and FTIR analyses, indicates that water was also present at a low temperature stage in the regolith's history. Possible precursor phases that the NWA 8114 goethite may have replaced under aqueous conditions include magnetite, maghemite or pyrite. Of the total iron oxides in NWA 8114, magnetite and maghemite make up 70% and 30% respectively (Agee et al., 2013). The goethite grains contain small amounts of Ti and S, consistent with precursor phases that contained some Ti-magnetite and pyrite.

A range of factors including temperature, pH, particle size, composition, concentration, structure and morphology can all play a part in the various possible interconversion reactions among the iron oxides. Studies suggest submicron magnetite and titanomagnetite oxidise rapidly to maghemite and goethite, whereas coarse-grained magnetite oxidises slowly to haematite (Xu et al., 1997; He and Traina, 2007). Magnetite (Fe_3O_4) will also transform to maghemite (Fe_2O_3) under hydrothermal conditions, and maghemite will then likely transform to haematite or goethite. Goethite may also form directly from magnetite via dissolution and reprecipitation (He and Traina, 2007). With silicate species, sulphate and/or Al present and lower pH, goethite formation will be promoted over magnetite or haematite (Cornell and Schwertmann, 2003). Lower temperatures favour goethite formation over hematite. Ferrihydrite, identified in NWA 7533 (Beck et al., 2015), could also potentially be an intermediate product of similar reactions.

If pyroxenes and Fe-Ti oxides such as magnetite in NWA 8114 were exposed to sulphurous hydrothermal fluids, then magnetite may have first been converted to pyrite (Wittmann et al., 2015; Lorand et al., 2015):

$$Fe_3O_4 + 6H_2S + O_2 \longrightarrow 3FeS_2 + 6H_2O \qquad \text{Equation 3}$$

Lorand et al. (2015) suggested this would occur at temperatures below 500 °C, from the maximum Ni contents and that pyrite formed on Mars as a late alteration mineral. They concluded the goethite they found in NWA 7533 was terrestrial alteration of the pyrite, with goethite postdating shock fractures in the pyrite and based on the D/H ratio of 10 ± 85‰ of five grains of Fe oxyhydroxides, via the following reaction

$$FeS_2 + 15\ O_2 + 10\ H_2O \longrightarrow 4\ FeO(OH) + 8\ H_2SO_4 \qquad \text{Equation 4}$$

A similar terrestrial origin for the NWA 8114 goethite clast is likely. Lorand et al. (2015) noted that the high-Ni concentration spots in NWA 7533 pyrite increase the weathering resistance, as seen by Ni-rich pyrite being less susceptible to alteration.

The oxygen isotope ratio of bulk NWA 7034 water suggests that most of it is extra-terrestrial, with $\Delta^{17}O$ above the terrestrial fractionation line (Agee et al., 2013). The bulk rock D/H isotope ratio of NWA 7034 water shows two distinct components, a negative value of about -100‰ likely to be terrestrial contamination, but also a positive value of 300‰ to 327‰. The latter is similar to the range of 250‰ to 900‰ values seen in the nakhlites though lower than those for shergottites of 1200‰ to 2100‰ or martian atmosphere at 4000‰ (Leshin et al., 1996), nevertheless it is clear there is some martian water within the breccia.

This leaves opens the possibility that the goethite formation and an associated phase of hydrous activity could have occurred on Mars. Goethite has been detected on Mars before by NASA's *Spirit* rover together with Fe^{3+}-sulphate at Gusev crater in the rocks at Columbia Hills on Mars, and this is one of the mineralogical lines of evidence of past aqueous processes (Ming et al., 2006; Morris et al., 2006).

4.2 Formation of Regolith Ejecta Blankets

NWA 7034 and its breccia pairs have been interpreted as fragments of impact regolith due to the meteoritic siderophiles (e.g., Ni, Ir) found in them. These indicate a component of at least a 3% carbonaceous chondrite material (Humayun et al., 2013; Wittmann et al., 2015). Thus, understanding the processes that create and change impact regolith on Mars are key to unravelling the evolution of NWA 8114. Here we seek to understand the mineralogical history of NWA 8114 in terms of the thermal evolution of an impact regolith on Mars.

During Mars' crustal evolution, with a past greater flux of impact events, regolith accumulated at a much faster rate than today (Golombek et al., 2006). On Mars the average surface impact velocity is 8.6 km s^{-1}, much lower than the Moon's average impact velocity of 16.2 km s^{-1} (Ivanov, 2001) so melting and vaporization should be less common on Mars than in the lunar regolith.

The thickness, t, of regolith ejecta blankets has been modelled from nuclear, terrestrial craters, lab experiments and estimates for lunar craters, and found for all of the examples to be a function of range:

$t = 0.14\ R^{0.74}\ (r/R)^{-3.0}$

where R is crater radius and r is range from the centre of the crater (McGetchin et al., 1973). Thus, a 20 km crater could create a 10 m thick ejecta blanket up to 50 km from the centre, a 50 km crater could create an ejecta blanket 100 m thick up to 80 km from the centre, and a 100 km crater could create a 200 m thick ejecta blanket up to 150 km from the centre.

A thick regolith layer can provide substantial insulation, which can maintain high temperatures at depth for long durations after impact events. Numerical modelling using HYDROTHERM showed that for a 100 km diameter crater on early Mars in the absence of fluid flow, isotherms over 900 °C can extend laterally for 10 km and persist for well over 4,000 years within the top 1 km of the crust (Abramov and Kring, 2005). A 30 km width crater is likely to have cooled below 400 °C within 25 years, whereas a 180 km crater would have temperatures over 900 °C extending 25 km, to nearly the crater rim in the top km depth, and over 1200 °C in the centre at 4000 years (Abramov and Kring, 2005).

4.3 Thermal Structure of the Martian Breccia Parental Regolith and Simple Cooling Model.

The properties of the martian regolith are important in constructing a thermal model for its evolution. Current surface temperatures on Mars range from -113 °C to -7 °C with an average of -58 °C at the equator (Carr, 2007) though may vary seasonally as much as from -153 °C at the poles to 20 °C at the equator. Thermal models require knowledge of crustal density, porosity with conductivity and ideally surface heat flow. The density of the crust has most recently been calculated as 2580 ± 210 kgm^{-3} from gravitational and topography measurements (Goossens et al., 2017), in good agreement with the uncompressed density of basalt of 2600 kg m^{-3} (Abramov and Kring, 2005). The heat capacity of basalt is 800 $Jkg^{-1}K^{-1}$ (Abramov and Kring, 2005), while Apollo soil has a value of 760 $Jkg^{-1}K^{-1}$ at 300 K (Ledlow et al., 1992). However, the geothermal gradients on Mars, including impact regolith terrains, are not well constrained as no surface heat flow measurements have yet been made. Babeyko and Zharkov (2000) did calculate a geothermal gradient of 13.5 ± 7.5 K/km based on a possible range of surface heat flow 30, 40 and 45 mWm^{-2}, and crustal thermal conductivity of 2.5 ± 0.5 $Wm^{-1}K^{-1}$. The authors based this model on the considered fraction of heat-producing radionuclides (K, Th, U) transported into the crust (Babeyko and Zharkov, 2000). The thermal conductivity of 2.5 $Wm^{-1}K^{-1}$ (Babeyko and Zharkov, 2000; Abramov and Kring, 2005) is also in good agreement with Robertson (1988), who noted that thermal conductivity varies as a function of $(1 - \text{porosity})^2$ for vesicular basalts. Thermal conductivity of 1.7 $Wm^{-1}K^{-}$ was used for ejecta and 2.5 W/mK for ice in modelling post-impact runoff at the Noachian Eberswalde crater (Mangold et al., 2012b). The porosity of the martian crust is modelled as decreasing exponentially with depth, starting with a value of

20% at the surface (Abramov and Kring, 2005). The sort of temperatures that the NWA 8114 parent regolith experienced would only be achieved at unrealistically great depths, within the mantle, unless there was an enhanced geothermal gradient resulting from the residual effects of the associated impact.

Studies of paired breccias have confirmed Cl-apatite U-Pb ages of 1.35-1.5 Ga (Yin et al., 2014; Bellucci et al., 2015; McCubbin et al., 2016). The U-Pb system for apatite has a low closure temperature of 450-500 °C, suggesting that the breccia must have experienced temperatures above 500 °C to reset them (Cherniak et al., 1991; Nemchin et al., 2009). Zircons have been divided into two age populations, both ancient (~4.4 Ga) and younger (1.4-1.7 Ga), with the suggestion that the younger metamict zircons experienced later alteration from low temperature fluids (Humayun et al., 2013; Yin et al., 2014; Nemchin et al., 2014; Bellucci et al., 2015; McCubbin et al., 2016). As many of the zircons have not been reset, the breccia could not have experienced temperatures above 900 °C (Ireland and Williams, 2003). Similarly, if temperatures had exceeded 900 °C then pyroxene exsolution textures seen would not have survived. The breccia is likely to have experienced high temperatures >700 °C for some time in order to have mobilised and melted feldspar-rich parts of the breccia, as evidenced by the incipient melting textures along the margin of feldspar veins within pyroxene clasts. Thus, a temperature range from 500 °C to 900 °C has been used in considering a thermal model that would allow the high temperature oxidation seen in pyroxene clasts, which is in agreement with a textural study of melting in the submicron matrix (McCubbin et al., 2016).

A simple cooling model has been constructed using Fourier's Law, which gives the cooling times from a starting temperature of 800 °C, for a 1 m thick slab of martian regolith, area 100 m^2, density 2600 kgm^{-3}, buried at two different depths, 5 m and 20 m (Fig. 19). The heat capacity used is 800 $Jkg^{-1}K^{-1}$, and two examples are shown using thermal conductivity of (A) 2.0 $Wm^{-1}K^{-1}$ and (B) 0.3 $Wm^{-1}K^{-1}$ based on lunar breccia samples (Weiss and Head, 2016). Radiative cooling has not been taken into account in this model but would lead to faster cooling rates than calculated.

Temperatures in the regolith at a burial depth of 5 m were maintained at >700 °C for over 28 days, which is sufficient for nanophase hematite to form (Minitti et al., 2002) (Fig. 19). Cooling from 800 °C at a depth of at least ~10 m maintains temperatures above 760 °C for 4 weeks, similar to the conditions needed to form analogous oxidation in enstatite (Straub et al., 1991). Oxidation was also reported in pigeonite samples oxidised in experiments at 700 °C for 7 days, but a larger effect was seen at 1000 °C for 14 days (Straub et al., 1991). This shows that even if the breccia formed close to the surface, in a relatively thin regolith blanket, of the order of 5 m deep, it would still experience elevated temperatures for weeks and up to months, consistent with the experimental results from pyroxene oxidation studies.

The cooling curves at 5 m depth or greater all maintain temperatures above 700 °C for at least six weeks, with a 20 m burial depth taking over twenty weeks to cool below this (Fig. 19). Thus, cooling at a depth of at least 5 m provides a thermal environment with temperatures high enough and cooling slow enough to produce the crystalline plagioclase seen in the veins.

5 CONCLUSIONS

The martian regolith breccia, NWA 8114 is paired with NWA 7034 and others. We have studied clasts within it using SEM, EPMA, FIB-STEM, synchrotron Fe-K XANES, XRD, XRF, FTIR and additionally, individual clasts have been separated and analysed with ^{40}Ar-^{39}Ar. This has revealed a combination of early magmatic events overprinted in some clasts by breakdown of pyroxene and feldspar veining at high temperature within the impact regolith.

- The NWA 8114 martian breccia includes a range of crystal clasts, including pyroxenes, plagioclase and alkali feldspar, with minor volumes of iron oxides, Cl-apatite, and also feldspar veins and aureoles. Pyroxene exsolution textures and feldspar cryptoperthite textures indicate slow cooling and a record of magmatic events prior to the impact-related processes.

- We have focused on the pyroxenes, investigating a texture where many pyroxene clasts contain sub-micron iron oxide grains and high porosity (~2 %). Some clasts have accreted rims, requiring time spent in an ejecta plume or density current, perhaps in the presence of water vapour, likely caused by the impact event that formed the breccia.

- FIB-TEM-EDX and XANES analyses reveal oxidation of up to 25% $Fe^{3+}/\Sigma Fe$ and the breakdown of clasts that were predominantly pyroxene, at high temperature, to iron oxide and a K-bearing feldspathic glassy material, with an associated porous texture. This was shown to be anhydrous by micro FTIR analyses, so any early water vapour was rapidly lost in the cooling regolith breccia on Mars. In one of these relict pyroxenes with a feldspar aureole, we used XRD to identify iron oxide as magnetite. This breakdown assemblage occurs in low-Ca pyroxene, relict pigeonite and some augite-dominated pyroxene clasts. The oxidation could arise from the loss of H^+ ions from the pyroxene structure, or the presence of transient water at the time of the impact event.

- The NWA 8114 parent rock was maintained at high temperature in the regolith. By analogy with published experimental studies, the oxidation and partial pyroxene breakdown are likely due to being held at a temperature above 700 °C for at least 7 days in an oxidising regolith environment as a result of the impact event. Temperatures above 700 °C would also be sufficient for *in-situ* melting of feldspar-rich domains forming feldspathic veins crosscutting the oxidised pyroxene. The area ~20 µm each side of the veins shows some textural evidence for partial melting and subsequent devitrification of the pyroxene host clasts. These could however, alternatively be hydrothermal feldspar veins, as a small amount of hyalophane is observed.

- A separated clast of augite showing the partial breakdown texture, yielded an approximate, maximum ^{40}Ar-^{39}Ar age of ~1.13 Ga to 1.25 Ga, in line with the 1.1 Ga to

1.4 Ga ages suggested by comparable studies. We interpret this age range as dating the pyroxene breakdown in the impact regolith at elevated temperatures of at least 700 °C.

- A simple cooling model suggests that the high temperature processing could have occurred within a regolith breccia of the order of ≥5 m depth.
- XRD, XANES and FTIR identify goethite, which is evidence of late stage low temperature hydrous alteration. In the absence of textural evidence to the contrary, this is probably the result of terrestrial alteration of martian pyrite.

6 ACKNOWLEDGEMENTS

We thank the Diamond Light Source beamline I-18 staff Fred Mosselmans and Konstantin Ignatyev and MIRIAM beamline B-22 staff Gianfelice Cinque and Mark Frogley for their help in data acquisition, during beam times sp10328-1 (December 2014), sm12761-1 (December 2015), sp13690-1 (July 2016), nt16688-1 (December 2016) and sp19641-1 (January 2018) that contributed to the results presented here. J.L. MacArthur, J.C. Bridges, and L.J. Hicks acknowledge funding from STFC to support this work. We thank John Holt, Graham Clark, Vinay Patel, Rob Wilson, Colin Cunningham, Lin Marvin, Tom Knott and Dan Smith from the University of Leicester for assistance with CT, SEM, TEM, EPMA operation and thin section preparation. Laura Paget is thanked for help with performing FTIR analyses. R.Burgess and K.Joy thank STFC (ST/M001253/1 and ST/L002957/1) and K.Joy also thanks a Royal Society University Research Fellowship (RS/UF140190) at the University of Manchester. R.H. Hewins and two anonymous reviewers are thanked for constructive reviews which helped improve the manuscript, as well as comments by P. Beck (associate editor).

7 REFERENCES

Abramov O. and Kring D. A. (2005) Impact-induced hydrothermal activity on early Mars. *J. Geophys. Res. Planets* **110**, E12S09.

Agee C. B., Wilson N. V., McCubbin F. M., Ziegler K., Polyak V. J., Sharp Z. D., Asmerom Y., Nunn M. H., Shaheen R., Thiemens M. H., Steele A., Fogel M. L., Bowden R., Glamoclija M., Zhang Z. and Elardo S. M. (2013) Unique Meteorite from Early Amazonian Mars: Water-Rich Basaltic Breccia Northwest Africa 7034. *Science* **339**, 780–785.

Babeyko A. Y. and Zharkov V. N. (2000) Martian crust: a modeling approach. *Phys. Earth Planet. Inter.* **117**, 421–435.

Basham M., Filik J., Wharmby M. T., Chang P. C. Y., El Kassaby B., Gerring M., Aishima J., Levik K., Pulford B. C. A., Sikharulidze I., Sneddon D., Webber M., Dhesi S. S., Maccherozzi F., Svensson O., Brockhauser S., Náray G. and Ashton A. W. (2015) Data Analysis WorkbeNch (DAWN). *J. Synchrotron Radiat.* **22**, 853–858.

Beck P., Pommerol A., Zanda B., Remusat L., Lorand J. P., Göpel C., Hewins R., Pont S., Lewin E., Quirico E., Schmitt B., Montes-Hernandez G., Garenne A., Bonal L., Proux O., Hazemann J. L. and Chevrier V. F. (2015) A Noachian source region for the "Black Beauty" meteorite, and a source lithology for Mars surface hydrated dust? *Earth Planet. Sci. Lett.* **427**, 104–111.

Bellucci J. J., Nemchin A. A., Whitehouse M. J., Humayun M., Hewins R. and Zanda B. (2015) Pb-isotopic evidence for an early, enriched crust on Mars. *Earth Planet. Sci. Lett.* **410**, 34–41.

Bibring J.-P., Langevin Y., Mustard J. F., Poulet F., Arvidson R., Gendrin A., Gondet B., Mangold N., Pinet P., Forget F., Berthé M., Bibring J.-P., Gendrin A., Gomez C., Gondet B., Jouglet D., Poulet F., Soufflot A., Vincendon M., Combes M., Drossart P., Encrenaz T., Fouchet T., Merchiorri R., Belluci G., Altieri F., Formisano V., Capaccioni F., Cerroni P., Coradini A., Fonti S., Korablev O., Kottsov V., Ignatiev N., Moroz V., Titov D., Zasova L., Loiseau D., Mangold N., Pinet P., Douté S., Schmitt B., Sotin C., Hauber E., Hoffmann H., Jaumann R., Keller U., Arvidson R., Mustard J. F., Duxbury T., Forget F. and Neukum G. (2006) Global Mineralogical and Aqueous Mars History Derived from OMEGA/Mars Express Data. *Science* **312**, 400–404.

Bouvier L. C., Costa M. M., Connelly J. N., Jensen N. K., Wielandt D., Storey M., Nemchin A. A., Whitehouse M. J., Snape J. F., Bellucci J. J., Moynier F., Agranier A., Gueguen B., Schönbächler M. and Bizzarro M. (2018) Evidence for extremely rapid magma ocean crystallization and crust formation on Mars. *Nature* **558**, 586–589.

Branney M. J. and Brown R. J. (2011) Impactoclastic Density Current Emplacement of Terrestrial Meteorite-Impact Ejecta and the Formation of Dust Pellets and Accretionary Lapilli: Evidence from Stac Fada, Scotland. *J. Geol.* **119**, 275–292.

Brown R. J., Branney M. J., Maher C. and Dávila-Harris P. (2010) Origin of accretionary lapilli within ground-hugging density currents: Evidence from pyroclastic couplets on Tenerife. *Geol. Soc. Am. Bull.* **122**, 305–320.

Carr M. H. (2007) *The Surface of Mars*., Cambridge University Press.

Cartwright J. A., Ott U., Herrmann S. and Agee C. B. (2014) Modern atmospheric signatures in 4.4 Ga Martian meteorite NWA 7034. *Earth Planet. Sci. Lett.* **400**, 77–87.

Cassata W. S., Cohen B. E., Mark D. F., Trappitsch R., Crow C. A., Wimpenny J., Lee M. R. and Smith C. L. (2018) Chronology of martian breccia NWA 7034 and the formation of the martian crustal dichotomy. *Sci. Adv.* **4**, eaap8306.

Changela H. G. and Bridges J. C. (2010) Alteration assemblages in the nakhlites: Variation with depth on Mars. *Meteorit. Planet. Sci.* **45**, 1847–1867.

Cherniak D. J., Lanford W. A. and Ryerson F. J. (1991) Lead diffusion in apatite and zircon using ion implantation and Rutherford Backscattering techniques. *Geochim. Cosmochim. Acta* **55**, 1663–1673.

Cinque G., Frogley M. D. and Bartolini R. (2011) Far-IR/THz spectral characterization of the coherent synchrotron radiation emission at diamond IR beamline B22. *Rendiconti Lincei* **22**, 33–47.

Cornell R. M. and Schwertmann U. (2003) *The Iron Oxides: Structure, Properties, Reactions, Occurrences and Uses.*, John Wiley & Sons.

Deer W. A., Howie R. A. and Zussman J. (2001) *Rock-forming Minerals: Feldspars, Volume 4A.*, Geological Society of London.

Ehlmann B. L., Mustard J. F., Clark R. N., Swayze G. A. and Murchie S. L. (2011a) Evidence for Low-Grade Metamorphism, Hydrothermal Alteration, and Diagenesis on Mars from Phyllosilicate Mineral Assemblages. *Clays Clay Miner.* **59**, 359–377.

Ehlmann B. L., Mustard J. F., Murchie S. L., Bibring J.-P., Meunier A., Fraeman A. A. and Langevin Y. (2011b) Subsurface water and clay mineral formation during the early history of Mars. *Nature* **479**, 53–60.

Gattacceca J., Rochette P., Scorzelli R. B., Munayco P., Agee C., Quesnel Y., Cournède C. and Geissman J. (2014) Martian meteorites and Martian magnetic anomalies: A new perspective from NWA 7034. *Geophys. Res. Lett.* **41**, 2014GL060464.

Gilbert J. S. and Lane S. J. (1994) The origin of accretionary lapilli. *Bull. Volcanol.* **56**, 398–411.

Goderis S., Brandon A. D., Mayer B. and Humayun M. (2016) Ancient impactor components preserved and reworked in martian regolith breccia Northwest Africa 7034. *Geochim. Cosmochim. Acta* **191**, 203–215.

Golombek M. P., Crumpler L. S., Grant J. A., Greeley R., Cabrol N. A., Parker T. J., Rice J. W., Ward J. G., Arvidson R. E., Moersch J. E., Fergason R. L., Christensen P. R., Castaño A., Castaño R., Haldemann A. F. C., Li R., Bell J. F. and Squyres S. W. (2006) Geology of the Gusev cratered plains from the Spirit rover transverse. *J. Geophys. Res. Planets* **111**, E02S07.

Goossens S., Sabaka T. J., Genova A., Mazarico E., Nicholas J. B. and Neumann G. A. (2017) Evidence for a low bulk crustal density for Mars from gravity and topography. *Geophys. Res. Lett.* **44**, 2017GL074172.

Gotić M. and Musić S. (2007) Mössbauer, FT-IR and FE SEM investigation of iron oxides precipitated from FeSO4 solutions. *J. Mol. Struct.* **834–836**, 445–453.

Graup G. (1981) Terrestrial chondrules, glass spherules and accretionary lapilli from the suevite, Ries Crater, Germany. *Earth Planet. Sci. Lett.* **55**, 407–418.

Gualtieri A. F. and Venturelli P. (1999) In situ study of the goethite-hematite phase transformation by real time synchrotron powder diffraction. *Am. Mineral.* **84**, 895–904.

Gulick S. P. S., Barton P. J., Christeson G. L., Morgan J. V., McDonald M., Mendoza-Cervantes K., Pearson Z. F., Surendra A., Urrutia-Fucugauchi J., Vermeesch P. M. and Warner M. R. (2008) Importance of pre-impact crustal structure for the asymmetry of the Chicxulub impact crater. *Nat. Geosci.* **1**, 131.

Hewins R. H., Zanda B., Humayun M., Nemchin A., Lorand J.-P., Pont S., Deldicque D., Bellucci J. J., Beck P., Leroux H., Marinova M., Remusat L., Göpel C., Lewin E., Grange M., Kennedy A. and Whitehouse M. J. (2017) Regolith breccia Northwest Africa 7533: Mineralogy and petrology with implications for early Mars. *Meteorit. Planet. Sci.* **52**, 89–124.

He Y. T. and Traina S. J. (2007) Transformation of magnetite to goethite under alkaline pH conditions. *Clay Miner.* **42**, 13–19.

Hicks L. J., Bridges J. C. and Gurman S. J. (2014) Ferric saponite and serpentine in the nakhlite martian meteorites. *Geochim. Cosmochim. Acta* **136**, 194–210.

Hicks L. J., MacArthur J. L., Bridges J. C., Price M. C., Wickham-Eade J. E., Burchell M. J., Hansford G. M., Butterworth A. L., Gurman S. J. and Baker S. H. (2017) Magnetite in Comet Wild 2: Evidence for parent body aqueous alteration. *Meteorit. Planet. Sci.* **52**, 2075–2096.

Huber M. S. and Koeberl C. (2017) Accretionary lapilli from the Sudbury impact event. *Meteorit. Planet. Sci.* **52**, 1257–1276.

Humayun M., Nemchin A., Zanda B., Hewins R. H., Grange M., Kennedy A., Lorand J.-P., Göpel C., Fieni C., Pont S. and Deldicque D. (2013) Origin and age of the earliest Martian crust from meteorite NWA 7533. *Nature* **503**, 513–516.

ICDD (2014) PDF-4/Minerals 2014 database, Int. Centre for Diffraction Data. Available at: http://www.icdd.com.

Ireland T. R. and Williams I. S. (2003) Considerations in Zircon Geochronology by SIMS. *Rev. Mineral. Geochem.* **53**, 215–241.

Ivanov B. A. (2001) Mars/Moon Cratering Rate Ratio Estimates. *Space Sci. Rev.* **96**, 87–104.

Johnson B. C. and Melosh H. J. (2014) Formation of melt droplets, melt fragments, and accretionary impact lapilli during a hypervelocity impact. *Icarus* **228**, 347–363.

Johnson M. C., Rutherford M. J. and Hess P. C. (1991) Chassigny petrogenesis: Melt compositions, intensive parameters and water contents of Martian (?) magmas. *Geochim. Cosmochim. Acta* **55**, 349–366.

Krogh T. E., McNutt R. H. and Davis G. L. (1982) Two high precision U–Pb zircon ages for the Sudbury Nickel Irruptive. *Can. J. Earth Sci.* **19**, 723–728.

Ledlow M. J., Zeilik M., Burns J. O., Gisler G. R., Zhao J.-H. and Baker D. N. (1992) Subsurface emissions from Mercury - VLA radio observations at 2 and 6 centimeters. *Astrophys. J.* **384**, 640–655.

Leroux H., Jacob D., Marinova M., Hewins R. H., Zanda B., Pont S., Lorand J.-P. and Humayun M. (2016) Exsolution and shock microstructures of igneous pyroxene clasts in the Northwest Africa 7533 Martian meteorite. *Meteorit. Planet. Sci.* **51**, 932–945.

Leshin L. A., Epstein S. and Stolper E. M. (1996) Hydrogen isotope geochemistry of SNC meteorites. *Geochim. Cosmochim. Acta* **60**, 2635–2650.

Lindsay F. N., Delaney J. S., Turrin B. D., Herzog G. F., Park J. and Swisher C. C. (2016) Ar Ages of Martian Meteorite Northwest Africa 7034. In Lunar and Planetary Science Conference. p. 3013. Available at: http://adsabs.harvard.edu/abs/2016LPI....47.3013L [Accessed April 5, 2016].

Lindsay F. N., Turrin B. D., Göpel C., Herzog G. F., Zanda B., Hewins R., Park J., Delaney J. S. and Swisher C. C. (2014) 40Ar/39Ar Ages of Martian Meteorite NWA 7533. In 77th Annual Meeting of the Meteoritical Society. p. 5383. Available at: http://adsabs.harvard.edu/abs/2014LPICo1800.5383L [Accessed October 30, 2017].

Lindsley D. H. and Andersen D. J. (1983) A two-pyroxene thermometer. *J. Geophys. Res. Solid Earth* **88**, A887–A906.

Liu Y., Ma C., Beckett J. R., Chen Y. and Guan Y. (2016) Rare-earth-element minerals in martian breccia meteorites NWA 7034 and 7533: Implications for fluid–rock interaction in the martian crust. *Earth Planet. Sci. Lett.* **451**, 251–262.

Lorand J.-P., Hewins R. H., Remusat L., Zanda B., Pont S., Leroux H., Marinova M., Jacob D., Humayun M., Nemchin A., Grange M., Kennedy A. and Göpel C. (2015) Nickeliferous pyrite tracks pervasive hydrothermal alteration in Martian regolith breccia: A study in NWA 7533. *Meteorit. Planet. Sci.* **50**, 2099–2120.

Mangold N., Carter J., Poulet F., Dehouck E., Ansan V. and Loizeau D. (2012a) Late Hesperian aqueous alteration at Majuro crater, Mars. *Planet. Space Sci.* **72**, 18–30.

Mangold N., Kite E. S., Kleinhans M. G., Newsom H., Ansan V., Hauber E., Kraal E., Quantin C. and Tanaka K. (2012b) The origin and timing of fluvial activity at Eberswalde crater, Mars. *Icarus* **220**, 530–551.

Marzo G. A., Davila A. F., Tornabene L. L., Dohm J. M., Fairén A. G., Gross C., Kneissl T., Bishop J. L., Roush T. L. and McKay C. P. (2010) Evidence for Hesperian impact-induced hydrothermalism on Mars. *Icarus* **208**, 667–683.

McCanta M. C. and Dyar M. D. (2017) Impact-related thermal effects on the redox state of Ca-pyroxene. *Meteorit. Planet. Sci.* **52**, 320–332.

McCubbin F. M., Boyce J. W., Novák-Szabó T., Santos A. R., Tartèse R., Muttik N., Domokos G., Vazquez J., Keller L. P., Moser D. E., Jerolmack D. J., Shearer C. K., Steele A., Elardo S. M., Rahman Z., Anand M., Delhaye T. and Agee C. B. (2016) Geologic history of Martian regolith breccia Northwest Africa 7034: Evidence for hydrothermal activity and lithologic diversity in the Martian crust. *J. Geophys. Res. Planets*, 2016JE005143.

McGetchin T. R., Settle M. and Head J. W. (1973) Radial thickness variation in impact crater ejecta: implications for lunar basin deposits. *Earth Planet. Sci. Lett.* **20**, 226–236.

Mckay D. S. and Morrison D. A. (1971) Lunar breccias. *J. Geophys. Res.* **76**, 5658–5669.

McSwiggen P. L., Morey G. B. and Cleland J. M. (1994) Occurrence and genetic implications of hyalophane in manganese-rich iron-formation, Cuyuna Iron Range, Minnesota, USA. *Mineral. Mag.* **58**, 387–399.

Melosh H. J. (2011) *Planetary Surface Processes.*, Cambridge University Press.

Ming D. W., Mittlefehldt D. W., Morris R. V., Golden D. C., Gellert R., Yen A., Clark B. C., Squyres S. W., Farrand W. H., Ruff S. W., Arvidson R. E., Klingelhöfer G., McSween H. Y., Rodionov D. S., Schröder C., de Souza P. A. and Wang A. (2006) Geochemical and mineralogical indicators for aqueous processes in the Columbia Hills of Gusev crater, Mars. *J. Geophys. Res. Planets* **111**, E02S12.

Minitti M. E., Mustard J. F. and Rutherford M. J. (2002) Effects of glass content and oxidation on the spectra of SNC-like basalts: Applications to Mars remote sensing. *J. Geophys. Res. Planets* **107**, 6–1.

Morris R. V., Klingelhöfer G., Schröder C., Rodionov D. S., Yen A., Ming D. W., de Souza P. A., Fleischer I., Wdowiak T., Gellert R., Bernhardt B., Evlanov E. N., Zubkov B., Foh J., Bonnes U., Kankeleit E., Gütlich P., Renz F., Squyres S. W. and Arvidson R. E. (2006) Mössbauer mineralogy of rock, soil, and dust at Gusev crater, Mars: Spirit's journey through weakly altered olivine basalt on the plains and pervasively altered basalt in the Columbia Hills. *J. Geophys. Res. Planets* **111**, E02S13.

Mosselmans J. F. W., Quinn P. D., Dent A. J., Cavill S. A., Moreno S. D., Peach A., Leicester P. J., Keylock S. J., Gregory S. R., Atkinson K. D. and Rosell J. R. (2009) I18 – the microfocus spectroscopy beamline at the Diamond Light Source. *J. Synchrotron Radiat.* **16**, 818–824.

Mustard J. F., Murchie S. L., Pelkey S. M., Ehlmann B. L., Milliken R. E., Grant J. A., Bibring J.-P., Poulet F., Bishop J., Dobrea E. N., Roach L., Seelos F., Arvidson R. E., Wiseman S., Green R., Hash C., Humm D., Malaret E., McGovern J. A., Seelos K., Clancy T., Clark R., Marais D. D., Izenberg N., Knudson A., Langevin Y., Martin T., McGuire P., Morris R., Robinson M., Roush T., Smith M., Swayze G., Taylor H., Titus T. and Wolff M. (2008) Hydrated silicate minerals on Mars observed by the Mars Reconnaissance Orbiter CRISM instrument. *Nature* **454**, 305–309.

Muttik N., McCubbin F. M., Keller L. P., Santos A. R., McCutcheon W. A., Provencio P. P., Rahman Z., Shearer C. K., Boyce J. W. and Agee C. B. (2014) Inventory of H2O in the ancient Martian regolith from Northwest Africa 7034: The important role of Fe oxides. *Geophys. Res. Lett.*, 8235–8244.

Nemchin A. A., Humayun M., Whitehouse M. J., Hewins R. H., Lorand J.-P., Kennedy A., Grange M., Zanda B., Fieni C. and Deldicque D. (2014) Record of the ancient martian hydrosphere and atmosphere preserved in zircon from a martian meteorite. *Nat. Geosci.* **7**, 638–642.

Nemchin A. A., Pidgeon R. T., Healy D., Grange M. L., Whitehouse M. J. and Vaughan J. (2009) The comparative behavior of apatite-zircon U-Pb systems in Apollo 14 breccias: Implications for the thermal history of the Fra Mauro Formation. *Meteorit. Planet. Sci.* **44**, 1717–1734.

Nyquist L. E., Shih C.-Y., McCubbin F. M., Santos A. R., Shearer C. K., Peng Z. X., Burger P. V. and Agee C. B. (2016) Rb-Sr and Sm-Nd isotopic and REE studies of igneous components in the bulk matrix domain of Martian breccia Northwest Africa 7034. *Meteorit. Planet. Sci.* **51**, 483–498.

Pan Y. and Fleet M. E. (1991) Barian feldspar and barian-chromian muscovite from the Hemlo area, Ontario. *Can. Mineral.* **29**, 481–498.

Poulet F., Bibring J.-P., Mustard J. F., Gendrin A., Mangold N., Langevin Y., Arvidson R. E., Gondet B., Gomez C., Berthé M., Erard S., Forni O., Manaud N., Poulleau G., Soufflot A., Combes M., Drossart P., Encrenaz T., Fouchet T., Melchiorri R., Bellucci G., Altieri F., Formisano V., Fonti S., Capaccioni F., Cerroni P., Coradini A., Korablev O., Kottsov V., Ignatiev N., Titov D., Zasova L., Pinet P., Schmitt B., Sotin C., Hauber E., Hoffmann H., Jaumann R., Keller U., Arvidson R., Mustard J. and Forget F. (2005) Phyllosilicates on Mars and implications for early martian climate. *Nature* **438**, 623–627.

Remusat L., Zanda B., Beck P., Lorand J.-P., Pont S., Leroux H. and Hewins R. (2015) New Constraints on the Water Budget in the Martian Breccia Meteorite NWA 7533. In 78th Annual Meeting of the Meteoritical Society. p. 5125. Available at: http://adsabs.harvard.edu/abs/2015LPICo1856.5125R [Accessed April 6, 2016].

Renne P. R., Balco G., Ludwig K. R., Mundil R. and Min K. (2011) Response to the comment by W.H. Schwarz et al. on "Joint determination of 40K decay constants and 40Ar∗/40K for the Fish Canyon sanidine standard,

and improved accuracy for 40Ar/39Ar geochronology" by P.R. Renne et al. (2010). *Geochim. Cosmochim. Acta* **75**, 5097–5100.

Robertson E. C. (1988) *Thermal properties of rocks*., U.S. Geological Survey,. Available at: http://pubs.er.usgs.gov/publication/ofr88441.

RRUFF Database (2006) Goethite R050142 - RRUFF Database: Raman, X-ray, Infrared, and Chemistry. Available at: http://rruff.info/Goethite/R050142 [Accessed June 15, 2016].

Ruzicka A., Grossman J., Bouvier A., Herd C. D. K. and Agee C. B. (2015) The Meteoritical Bulletin, No. 101. *Meteorit. Planet. Sci.* **50**, 1661–1661.

Santos A. R., Agee C. B., McCubbin F. M., Shearer C. K., Burger P. V., Tartèse R. and Anand M. (2015) Petrology of igneous clasts in Northwest Africa 7034: Implications for the petrologic diversity of the martian crust. *Geochim. Cosmochim. Acta* **157**, 56–85.

Schmieder M., Kennedy T., Jourdan F., Buchner E. and Reimold W. U. (2018) A high-precision 40Ar/39Ar age for the Nördlinger Ries impact crater, Germany, and implications for the accurate dating of terrestrial impact events. *Geochim. Cosmochim. Acta* **220**, 146–157.

Schumacher R. and Schmincke H.-U. (1995) Models for the origin of accretionary lapilli. *Bull. Volcanol.* **56**, 626–639.

Schwenzer S. P. and Kring D. A. (2009) Impact-generated hydrothermal systems capable of forming phyllosilicates on Noachian Mars. *Geology* **37**, 1091–1094.

Siegert S., Branney M. J. and Hecht L. (2017) Density current origin of a melt-bearing impact ejecta blanket (Ries suevite, Germany). *Geology* **45**, 855–858.

Stöffler D. and Grieve R. A. F. (2007) *Impactites. In: Metamorphic Rocks: A Classification and Glossary of Terms - Cambridge University Press*. edited by Fettes D. and Desmons J. Cambridge, UK., Cambridge University Press. Available at: http://www.cambridge.org/catalogue/catalogue.asp?isbn=9780521336185&ss=toc [Accessed June 29, 2017].

Straub D. W., Burns R. G. and Pratt S. F. (1991) Spectral signature of oxidized pyroxenes: implications to remote sensing of terrestrial planets. *J. Geophys. Res. Planets* **96**, 18819–18830.

Takenouchi A., Mikouchi T. and Kogure T. (2017) Mineralogical study of brown olivine in Northwest Africa 1950 shergottite and implications for the formation mechanism of iron nanoparticles. *Meteorit. Planet. Sci.* **52**, 2491–2504.

Turner S. M. R., Bridges J. C., Grebby S. and Ehlmann B. L. (2016) Hydrothermal activity recorded in post Noachian-aged impact craters on Mars. *J. Geophys. Res. Planets* **121**, 2015JE004989.

Udry A., Lunning N. G., McSween Jr. H. Y. and Bodnar R. J. (2014) Petrogenesis of a vitrophyre in the martian meteorite breccia NWA 7034. *Geochim. Cosmochim. Acta* **141**, 281–293.

VG (2017) *VG Studio Max.*, Volume Graphics. Available at: https://www.volumegraphics.com/en/products/vgstudio-max.html [Accessed January 26, 2018].

Warren P. H. and Rubin A. E. (2010) Pyroxene-selective impact smelting in ureilites. *Geochim. Cosmochim. Acta* **74**, 5109–5133.

Wechsler B. A., Lindsley D. H. and Prewitt C. T. (1984) Crystal structure and cation distribution in titanomagnetites (Fe (sub 3-x) Ti $_x$ O $_4$). *Am. Mineral.* **69**, 754–770.

Weiss D. K. and Head J. W. (2016) Impact ejecta-induced melting of surface ice deposits on Mars. *Icarus* **280**, 205–233.

Wittmann A., Korotev R. L., Jolliff B. L., Irving A. J., Moser D. E., Barker I. and Rumble D. (2015) Petrography and composition of Martian regolith breccia meteorite Northwest Africa 7475. *Meteorit. Planet. Sci.* **50**, 326–352.

Xu W., Van der Voo R., Peacor D. R. and Beaubouef R. T. (1997) Alteration and dissolution of fine-grained magnetite and its effects on magnetization of the ocean floor. *Earth Planet. Sci. Lett.* **151**, 279–288.

Yancey T. E. and Guillemette R. N. (2008) Carbonate accretionary lapilli in distal deposits of the Chicxulub impact eventChicxulub carbonate lapilli. *GSA Bull.* **120**, 1105–1118.

Yin Q. Z., McCubbin F. M., Zhou Q., Santos A. R., Tartèse R., Li X., Li Q., Liu Y., Tang G., Boyce J. W., Lin Y., Yang W., Zhang J., Hao J., Elardo S. M., Shearer C. K., Rowland D. J., Lerche M. and Agee C. B. (2014) An Earth-like beginning for ancient Mars indicated by alkali-rich volcanism at 4.4 Ga. *LPSC XLV* **Abstract #1320**. Available at: http://www.hou.usra.edu/meetings/lpsc2014/pdf/1320.pdf.

Zak L. (1991) Hyalophane-zoisite veins from the pyrite- rhodochrosite deposits near Litosice in eastern Bohemia (Czechoslovakia). *Cas. Miner. Geol* **36**, 67–75.

Zhu D., CUI Y., HAPUGODA S., VINING K. and PAN J. (2012) Mineralogy and crystal chemistry of a low grade nickel laterite ore. *Trans. Nonferrous Met. Soc. China* **22**, 907–916.

8 LIST OF TABLES AND FIGURES

Table 1. Different classifications of clasts within the martian breccias as described by different authors.

Table 2: Representative SEM-EDX and EPMA compositions of the relict pigeonite clast with feldspar veins (Fig. 6A), the goethite clast (Fig. 7B), the pyroxene exsolution clast (Fig. 4F) and clasts 1, 2 (plagioclase = plag) and 3 (augite with plagioclase inclusions), dated with ^{40}Ar-^{39}Ar (Fig. 10).

Table 3: Representative TEM-EDX compositions of the pyroxenes studied, given in oxide weight % normalized to 100%.

Table 4: Pre-edge centroid and Fe-K edge energies shown in Fig. 13G, H, and Fig. 14.

Table 5: XRD measured *d*-spacings (Å) for indices *hkl*, as plotted in Fig. 15, with calculated unit cell dimensions *a, b, c* (Å). Measurements from the XRD map in the iron oxide grain (Fig. 7D, black box, C5), XRD point measurements across the relict pyroxene (px) with feldspar aureole showing sub-micron iron oxide grains (Fig. 7A, X1-X5) and the low-Ca relict pyroxene with feldspar aureole showing sub-micron iron oxide grains (C29, Fig. 4G) and reference standards.

Fig. 1. (A) Main mass of NWA 8114 (~1.5 g) with visible clasts up to 0.5 mm in size. (B) A CT image of a slice from the middle of the NWA 8114 main mass, showing a 1.5 mm diameter spherule with concentric structure and layers.

Fig. 2. (A) BSE image of section A of NWA 8114 showing varied clasts in the fine grained matrix. The black box denotes part of a large predominantly relict pigeonite clast where two FIB-TEM sections were taken (Fig. 12), the white box shows the area examined with Fe-K XANES (Fig. 13). Veins can be seen cutting the relict pigeonite clast and the partially melted accreted rim (white dotted line). (B) Mineral Liberation Analysis (MLA) map of the right hand side of section A. (C) Part of the accreted rim indicated by the white dotted line in A, shown at higher resolution with evidence of melting.

Fig. 3. Standardised EDS, combined X-ray element map of section C, where Fe=red, Ca=green, Al=blue. Thus, pyroxenes are dark green, iron oxides are red, plagioclase light blue, K-feldspar dark blue, Cl-apatite bright green. The black clasts are mostly Mg-rich pyroxene. The relict pyroxene with feldspar aureole, containing a goethite clast (Fig. 7), is shown by the white ellipse.

Fig. 4. Clasts from polished sections of NWA 8114, scale bars all 50 μm, white rectangles show FIB-TEM section locations (Fig. 11, Table 3). Px=pyroxene, pl=plagioclase, or=orthoclase, mag=magnetite, aug=augite, pig=pigeonite, py=pyrite. (A) Relict pyroxene $En_{53}Fs_{19}Wo_{28}$ with iron oxide grains (arrows), porosity and plagioclase $An_{25\text{-}55}Ab_{44\text{-}75}$ aureole, showing concave outer surfaces (FIB6). (B) Low-Ca relict pyroxene $En_{72}Fs_{26}Wo_{2}$ with iron oxide grains (arrows), porosity and $An_{40\text{-}52}Ab_{43\text{-}56}Or_{3\text{-}4}$ plagioclase aureole (FIB7). (C) Ti-rich magnetite core intergrowth with magnetite rim. (D) Bulk pigeonite $En_{44}Fs_{50}Wo_{6}$ with augite $En_{37}Fs_{26}Wo_{37}$ exsolution. (E) Bulk augite $En_{31}Fs_{24}Wo_{45}$ with pigeonite $En_{36}Fs_{47}Wo_{17}$ exsolution. (F) Bulk

pigeonite $En_{52}Fs_{43}Wo_5$ with augite $En_{42}Fs_{18}Wo_{40}$ exsolution with iron oxide grains. (G) Low-Ca $En_{68}Fs_{30}Wo_2$ relict pyroxene with iron oxide grains, porosity and $An_{32-48}Ab_{49-63}Or_{2-5}$ plagioclase aureole (FIB2). (H) Cryptoperthite $An_{2-10}Ab_{8-95}Or_{3-91}$ feldspar. (I) Small pyrite inclusion in magnetite.

Fig. 5. (A) BSE image of an exsolution pyroxene clast, pigeonite composition $En_{41}Fs_{53}Wo_6$, augitic lamellae $En_{33}Fs_{26}Wo_{41}$ (C26, Fig. 8). (B) XRF map of the white box area in (A) showing Ca (green) and Fe (red) at 2 μm per pixel resolution.

Fig. 6. BSE images of the large relict pigeonite clast from Fig. 2 showing (A) veins containing plagioclase feldspar. (B) Close up of the white box region from A, showing the partial melting beside the vein. (C) SEM-EDX spectra for locations 1-6 shown in A and B: (1) An area of feldspar $An_{18}Ab_{55}Or_{27}$ in the vein. (2) A point measurement of orthoclase $Ab_{13}Or_{87}$ in the vein. (3) An area of pigeonite with iron oxide grains (white). (4) Bulk composition of ~20 μm region each side of the vein containing (5) light grey stoichiometric pyroxene $En_{37}Fs_{42}Wo_{21}$ and (6) dark dendrites relatively enriched in Al, Na and K and depleted in Mg and Fe compared with the pyroxene.

Fig. 7. BSE images of (A) Relict pyroxene ($En_{41-48}Wo_{26-39}Fs_{17-29}$), with plagioclase aureole ($Ab_{51-65}An_{18-40}Or_{2-22}$) and iron oxide grains. The black box highlights the goethite inclusion shown in B; the white box area was examined with Fe-K XANES (Fig. 13) and the X1-X5 points show XRD measurement locations (Table 5). (B) Goethite (gt) grain cross cut by calcium carbonate veins, with Cl-apatite (ap) inclusion. (C) Standardised EDS, combined X-ray element false-colour element distribution map of A, Fe = red, Ca=green, Al=blue. (D) 5 μm synchrotron XRF map of the goethite grain, with the location of the XRD map (black rectangle) and XANES measurements (X), Fe is red, Ca is green, Ni is blue.

Fig. 8. Pyroxene quadrilateral showing: (1) the augite-pigeonite compositions in exsolution clasts with dotted tie lines overlaid on crystallisation temperatures showing a range of crystallisation temperatures from 900 to 1050 °C (Lindsley and Andersen, 1983), measured with EPMA (diamonds) or where lamellae were too narrow, measured with SEM (squares). (2) Monomineralic pyroxene clasts compositions (black diamonds). (3) FIB section compositions from pyroxene clasts showing breakdown measured with TEM-EDX (circles), also shown in Table 3.

Fig. 9. Mineral compositions of feldspars, showing similarity between plagioclase in the veins, the plagioclase bordering pyroxene clasts (Fp borders), and in monomineralic plagioclase clasts. The K-rich feldspar clast compositions also match the K-rich feldspar found in the veins.

Fig. 10. (A) BSE image of part of the poorly polished augite clast 3 analysed with ^{40}Ar-^{39}Ar in Fig. 17, showing predominantly augite (aug) $En_{24-39}Fs_{13-26}Wo_{48-50}$, plagioclase (pl) inclusions, $An_{12-84}Ab_{15-74}Or_{0-17}$ and a calcite vein. (Inset) Microscope image of part of clast 3, showing a rim

and green pyroxene. (B) BSE image of augite shown in A (white rectangle) showing porosity (black) and iron oxide grains (white).

Fig. 11. (A) TEM bright field image of FIB1 taken from the relict pigeonite clast (Fig. 2A). (B) STEM bright field image of FIB7 taken from the relict pyroxene (px) $En_{72}Fs_{26}Wo_2$ shown in Fig. 4B, showing iron oxide (iron ox), porosity and a granoblastic texture with ~120° grain boundaries.

Fig. 12. (A) Black box area from Fig. 2 showing altered relict pigeonite $En_{30-33}Fs_{49-59}Wo_{11-18}$ with fine iron oxide and feldspar grains. (B) FIB-TEM section FIB3 taken from the location shown in A. (C) BF STEM image of the white box area in B showing iron oxide (iron ox), pigeonite (pg), augite (aug) and aluminium silicate (AlSi). (D) BF-TEM image showing pigeonite and aluminium silicate. (E) BF-TEM image of iron oxide grain.

Fig. 13. (A) BSE image of part of the relict pigeonite clast (Fig. 2A white box) where a Fe-K XANES map was taken. (B) Fe-K XANES map, 65 × 450 μm (5 μm resolution), showing normalized intensity measured at 7120.0 eV, light areas = Fe^{2+}, dark areas = Fe^{3+}. (C) 2 μm XRF image of XANES area, Fe=red, Ca=green, Ti=blue. (D) BSE image of part of the relict pyroxene with feldspar aureole (Fig. 7A, white box) where a Fe-K XANES map was taken. (E) Fe-K XANES map, 40 × 640 μm (5 μm resolution), showing normalized intensity measured at 7120.0 eV, light areas = Fe^{2+}, dark areas = Fe^{3+}. (F) 5 μm XRF image of XANES area, Fe=red, Ca=green, Ti=blue. (G) Typical normalized Fe-K edges for a homogenous pyroxene (px) clast, the pyroxene clast with feldspar aureole in area E, the relict pigeonite clast area B, and the augite clast from Fig. 10. Inset shows the pre-edge $1s \rightarrow 3d$ centroid for each of the four. For energy values, see Table 4. (H) Normalised Fe-K edges for NWA 8114 C5 goethite grain versus standards. Inset shows the pre-edge $1s \rightarrow 3d$ centroid. For energy values, see Table 4.

Fig. 14. Pre-edge centroid vs. Fe-K edge energies for monomineralic pyroxene clasts; pyroxene in the relict pyroxene (px) clast and relict pyroxene clast with feldspar (fp) aureole (Fig. 13G); a low-Ca relict pyroxene with feldspar aureole C29 (Fig. 4G); a high-Ca relict pyroxene with feldspar aureole B202 (Fig. 4A); goethite (Fig. 7B); iron oxides, pyrite, and Ti-magnetite (Fig. 4C) from NWA 8114, and standards (including San Carlos olivine). For energy values, see Table 4.

Fig. 15. XRD d-spacing peaks for (A) a goethite standard, two data points from the XRD map taken across the goethite grain in Fig. 7B (C5-7, C5-32), 'X4' shown in Fig. 7A, and the five expected most intense goethite peaks (dashed lines) (Gualtieri and Venturelli, 1999). (B) a magnetite standard, four of the five data points 'X' shown in Fig. 7A, and the five expected most intense magnetite peaks (dotted lines) (Wechsler et al., 1984). (C) four pyroxene and two feldspar clasts (two shown in Fig. 4GH) with the five expected most intense magnetite peaks (dotted lines) (Wechsler et al., 1984). (D) Calculated unit cell dimensions *a, b, c* (Å) plotted for d-spacing values from the XRD map data for the goethite grain (black diamonds) and our

goethite standard (squares) with error bars, and goethite standards from the ICDD database (white circles) (ICDD, 2014). For data values, see Table 5.

Fig. 16. Reflectance absorption of 9 measurements taken from a map across the goethite grain (solid line) in the relict pyroxene with feldspar aureole (Fig. 7B). The dotted vertical lines show the characteristic absorption peaks for goethite at 3145 cm^{-1} (Beck et al., 2015), 895 cm^{-1} and 795 cm^{-1} (Gotić and Musić, 2007), whereas the relict pyroxene (px) clast (dotted) (Fig. 2) and the rest of the relict pyroxene with feldspar (fp) aureole (dashed) (Fig. 7A) show no evidence of H_2O or –OH groups in this region.

Fig. 17. ^{40}Ar-^{39}Ar laser age determinations of clasts (1, 2 and 4 feldspar; 3 augite) showing (A) age and (B) Ca/K spectra. See data in Table A1. These data are uncorrected for any trapped martian atmospheric component. As a result we use the maximum approximate ages from these data i.e. 1130-1250 Ma for the augite clast. The apparent ages for the feldspar clasts are too disturbed to give an age.

Fig. 18. Reported ages for bulk rock and mineral separates from pairs of NWA 8114. Coloured rectangles represent age and 2σ uncertainty for [1]Agee et al. (2013), [3]Nyquist et al. (2016), [4]Bouvier et al. (2018), [5]Yin et al. (2014), [7]McCubbin et al. (2016), [8]Bellucci et al. (2015), [9]Liu et al. (2016), [10]Cassata et al. (2018), 1σ uncertainty for [6]Humayun et al. (2013), [11]Lindsay et al. (2014), [12]Lindsay et al. (2016) and the upper limit for the age from [2]Cartwright et al. (2014) and uncorrected ages, 1130 Ma to 1250 Ma, for the Ar-Ar dating of the augite clast in this study[13].

Fig. 19: Modelled cooling profiles using Fourier's law for a 1 m thick slab of martian regolith with surface area 100 m^2, density 2600 kgm^{-3} buried at two different depths, 5 m and 20 m, starting at 800 °C. The martian surface temperature is assumed as -60 °C. The heat capacity used is 800 $Jkg^{-1}K^{-1}$, the effect of varying this by ±10% or ±40% is shown by the dark grey and light grey areas respectively. Thermal conductivity is estimated as (A) 2.0 $Wm^{-1}K^{-1}$ based on basalt values and (B) 0.3 $Wm^{-1}K^{-1}$ based on lunar breccia values (Weiss and Head, 2016). (C) Detailed cooling profiles with parameters the same as (B) over the first 20 weeks compared with oxidation studies showing nanophase hematite forming in pigeonite, enstatite (Straub et al., 1991) and analogue martian samples (Minitti et al., 2002). As some of the zircons have not been reset by the breccia formation event at ~1.25 Ga and there is not extensive evidence of melting in the matrix, it is unlikely that temperatures exceeded 900 °C (orange area). As Cl-apatite grains have had their U-Pb system reset 1.35 - 1.5 Ga (Yin et al., 2014; Bellucci et al., 2015; McCubbin et al., 2016), temperatures must have exceeded 500 °C (green area). This model shows a burial depth of ~5 m would be sufficient to provide enough heat to partially oxidise the pyroxene and produce the micron and submicron grains of magnetite observed.

9 APPENDIX

Table A1: ^{40}Ar-^{39}Ar analytical data for NWA 8114 clasts (1, 2 and 4 feldspar; 3 augite).

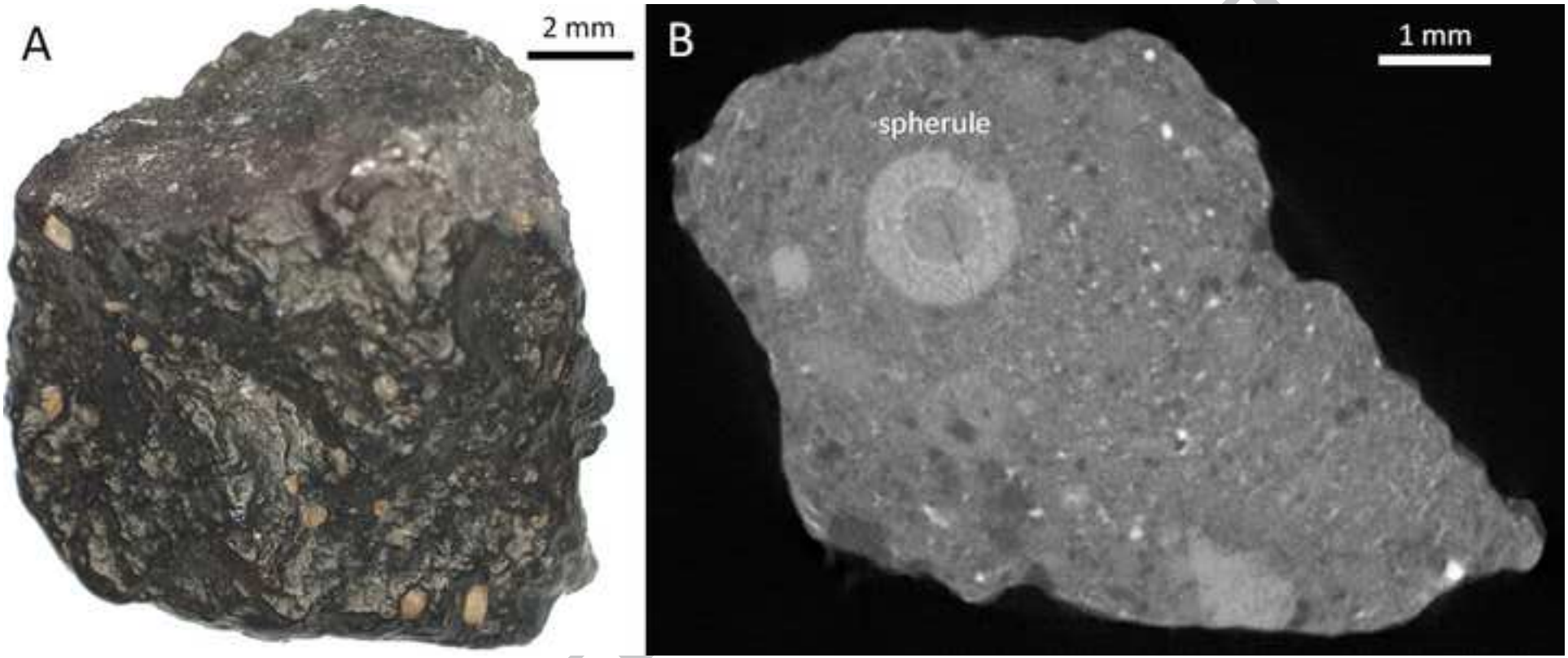

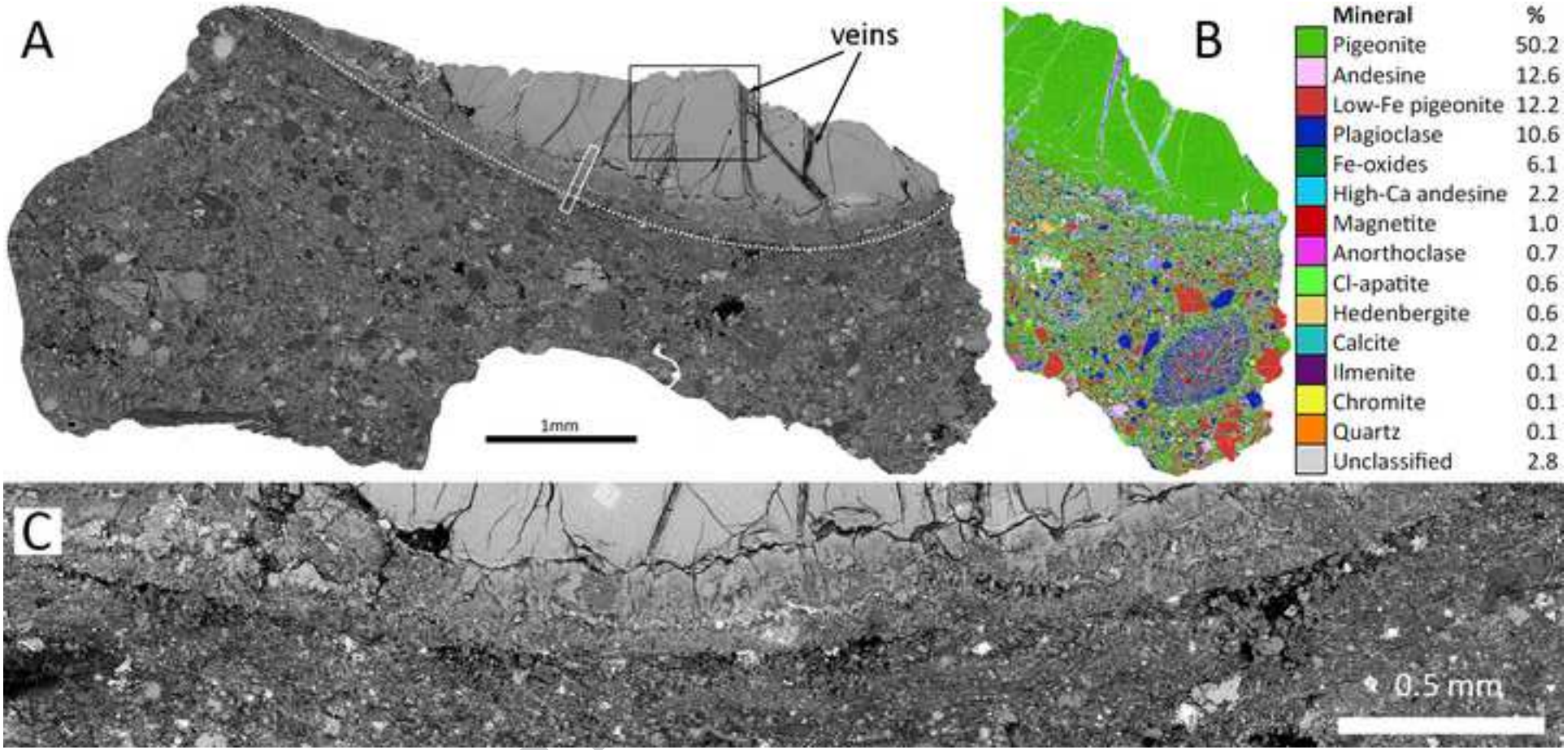

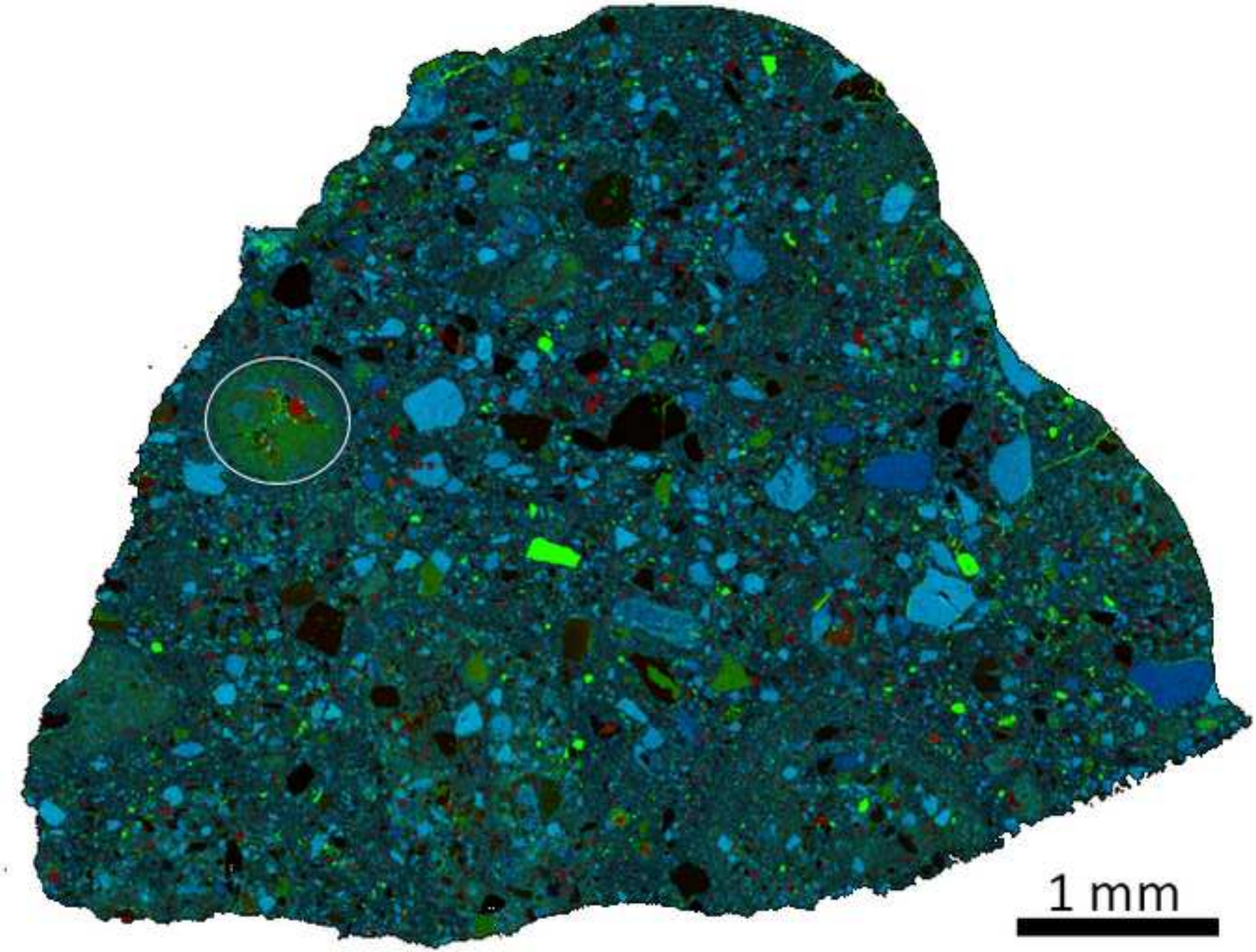

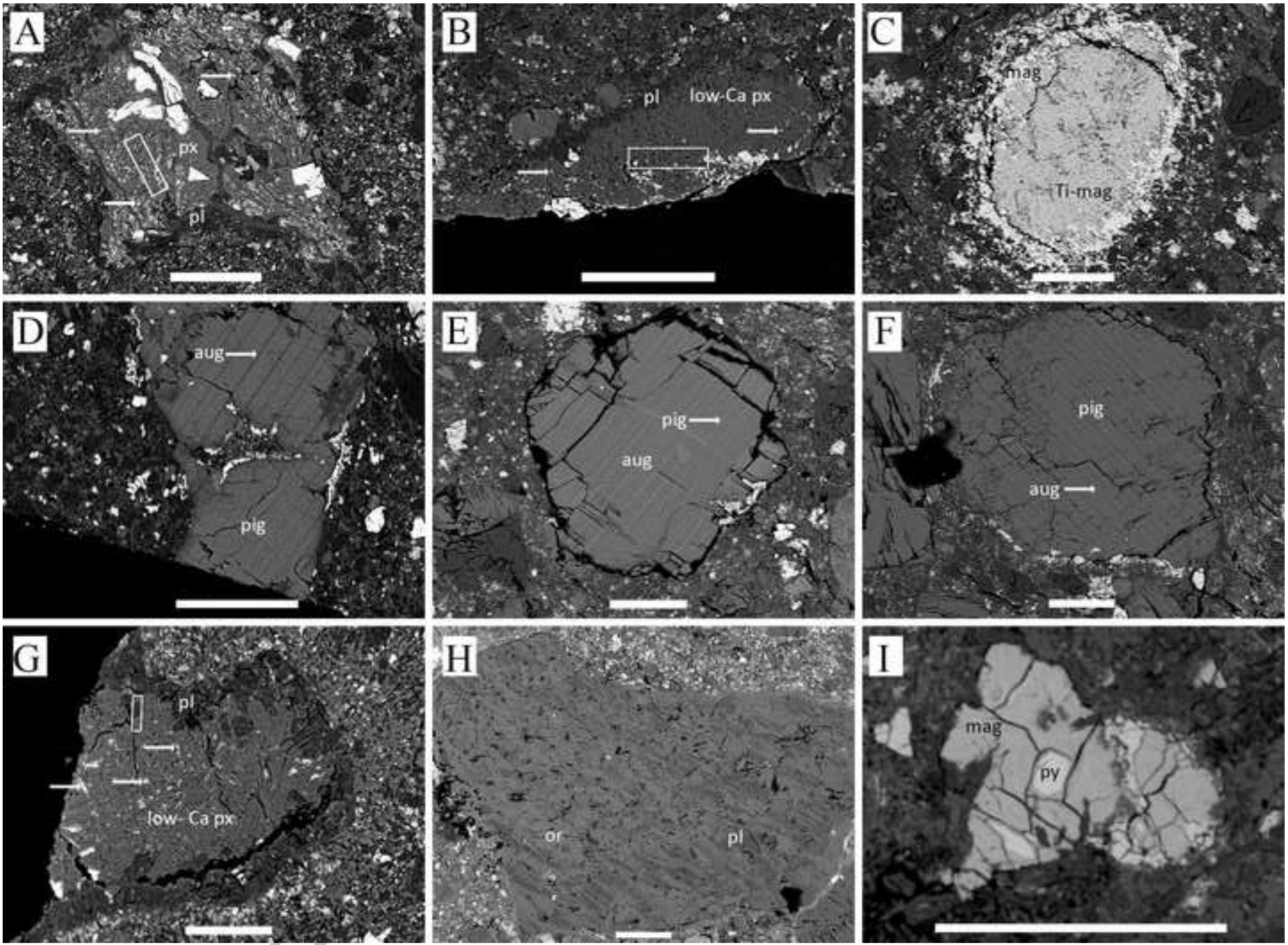

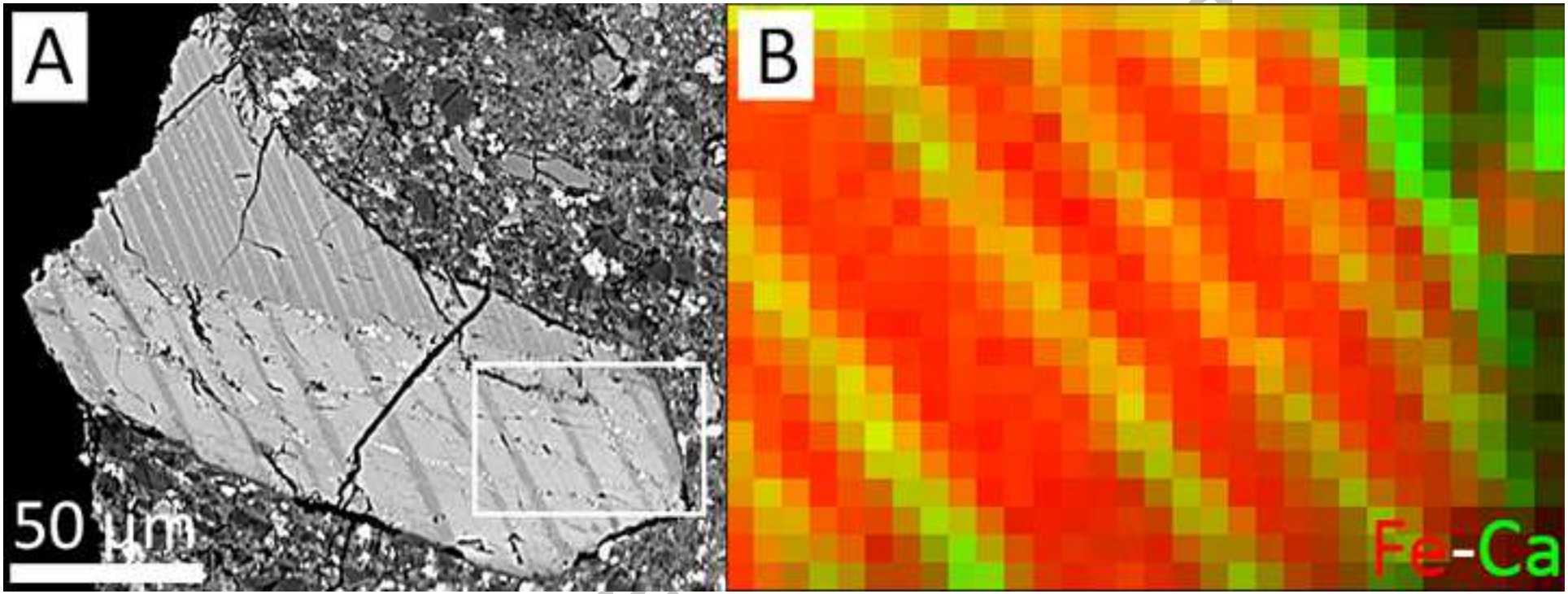

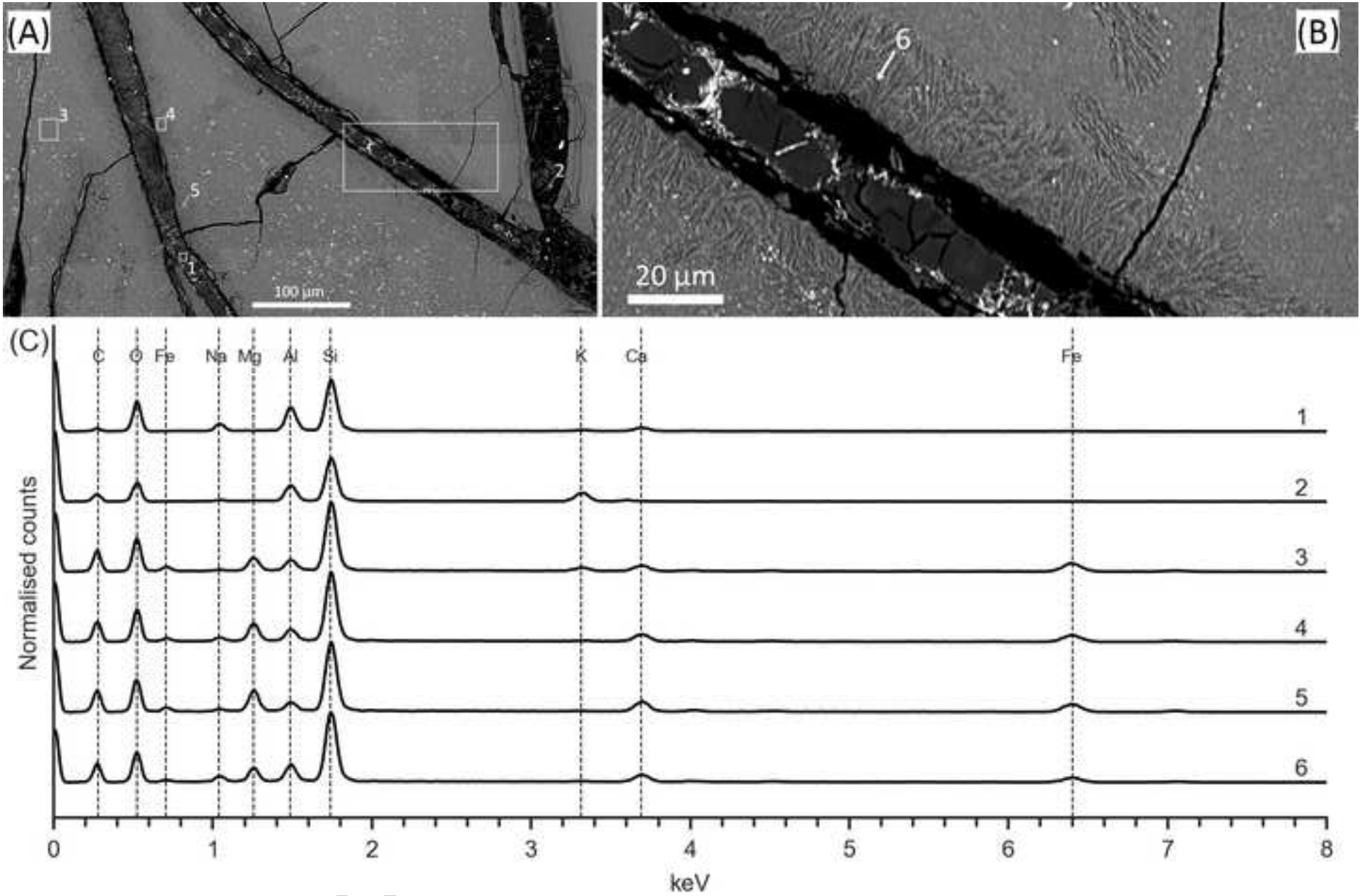

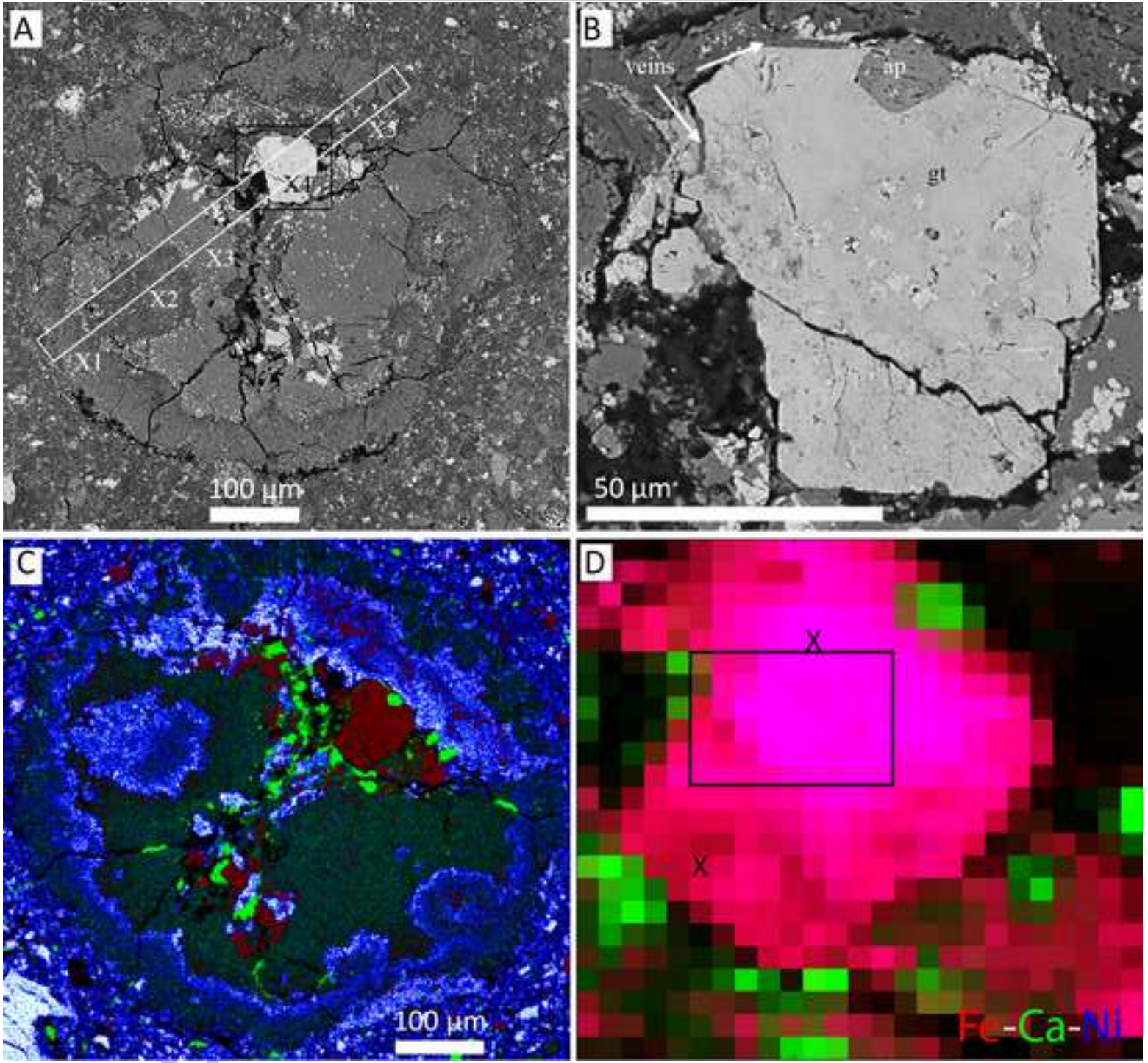

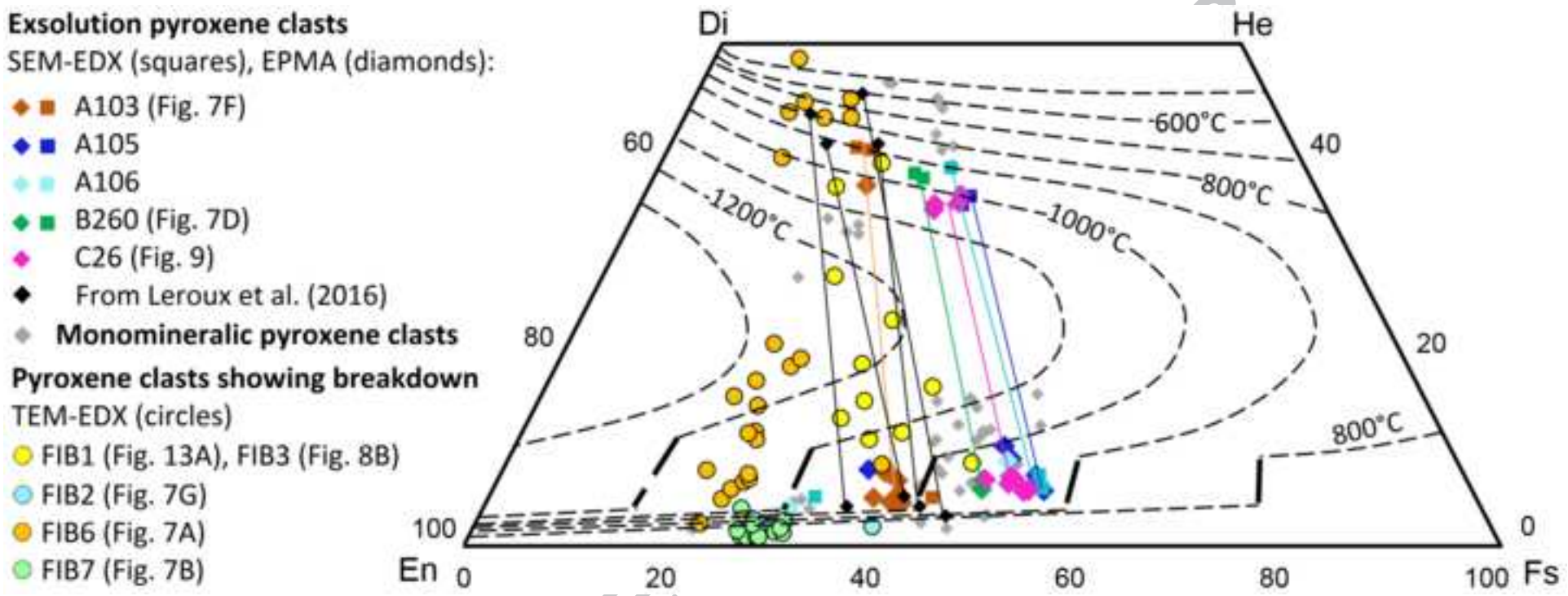

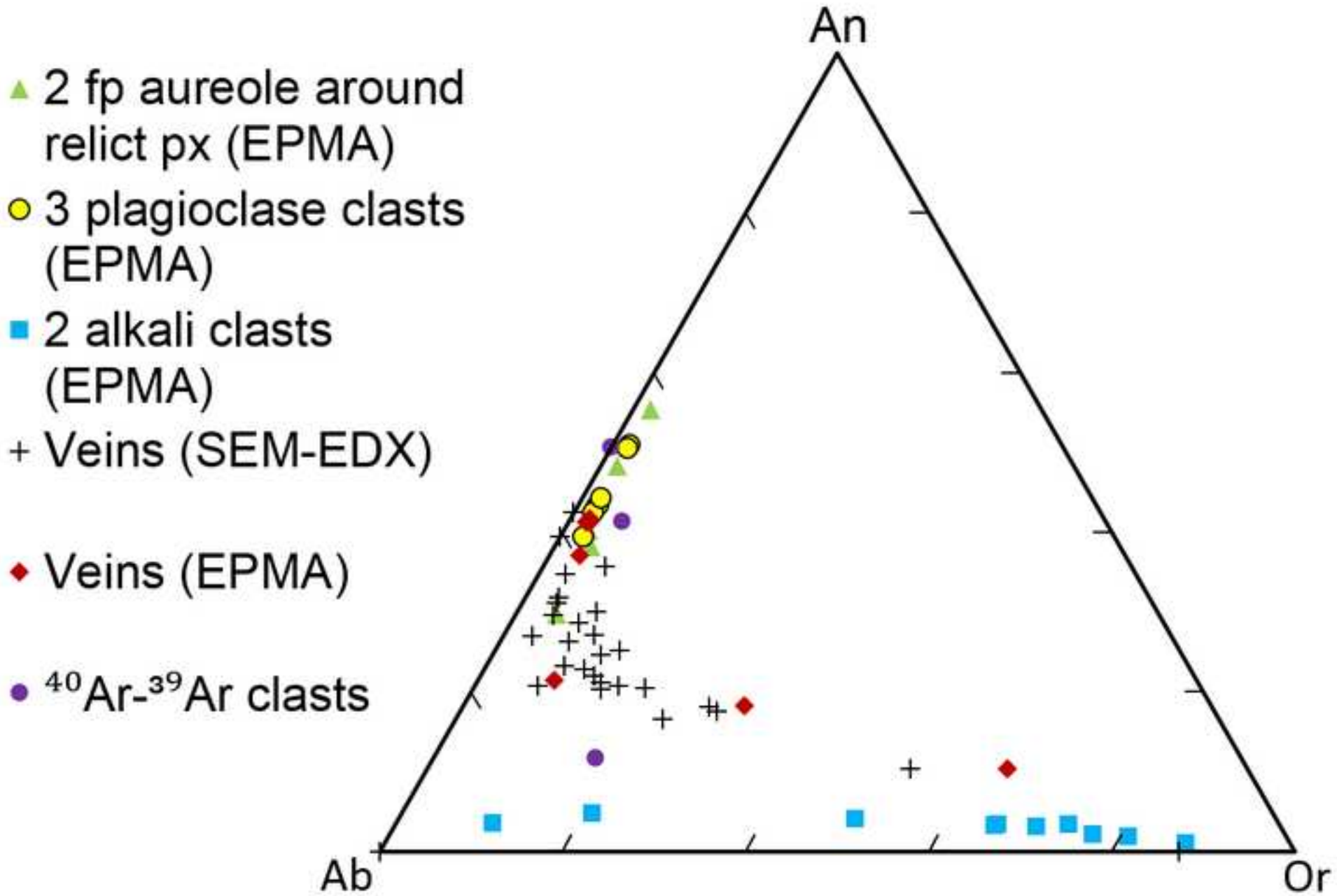

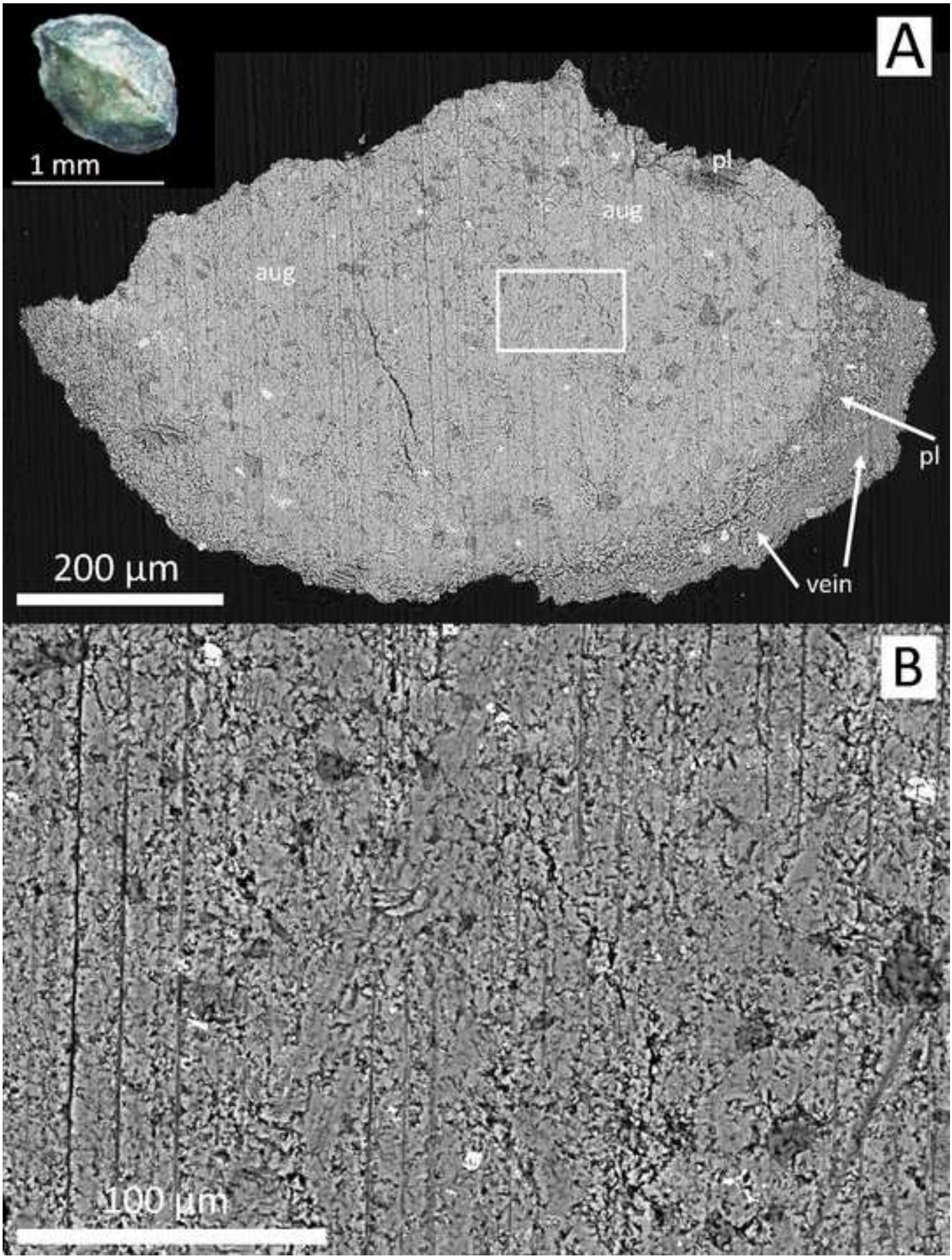

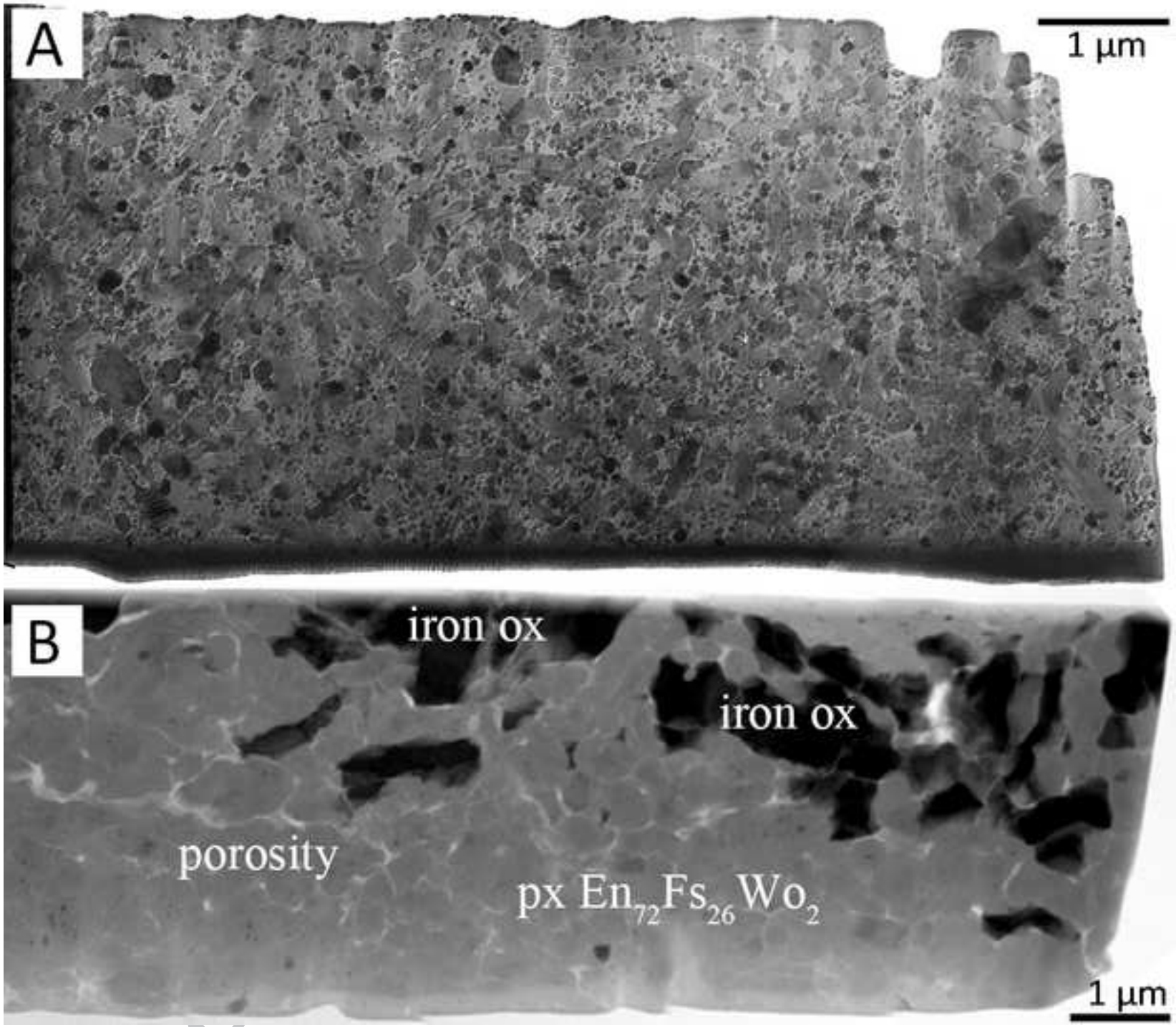

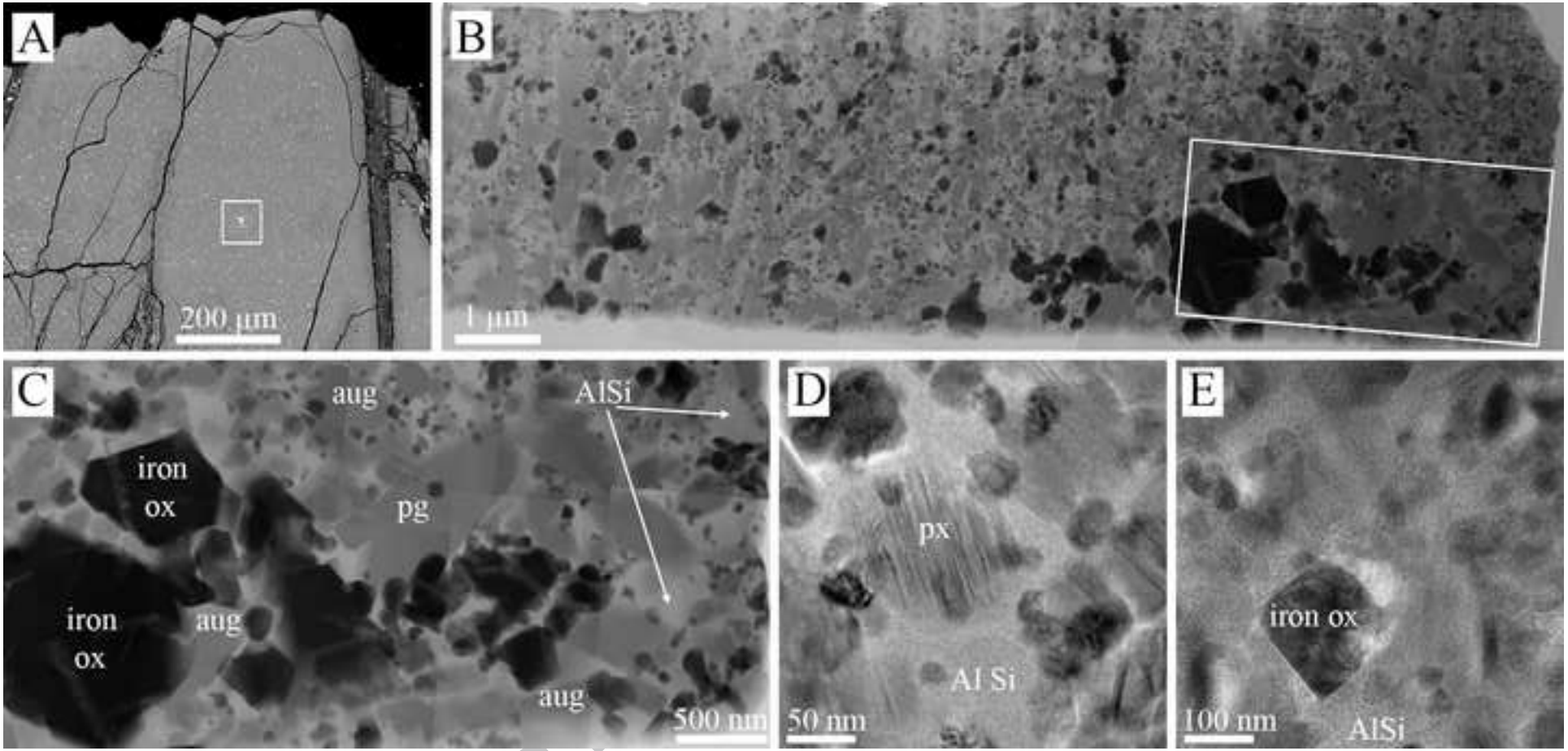

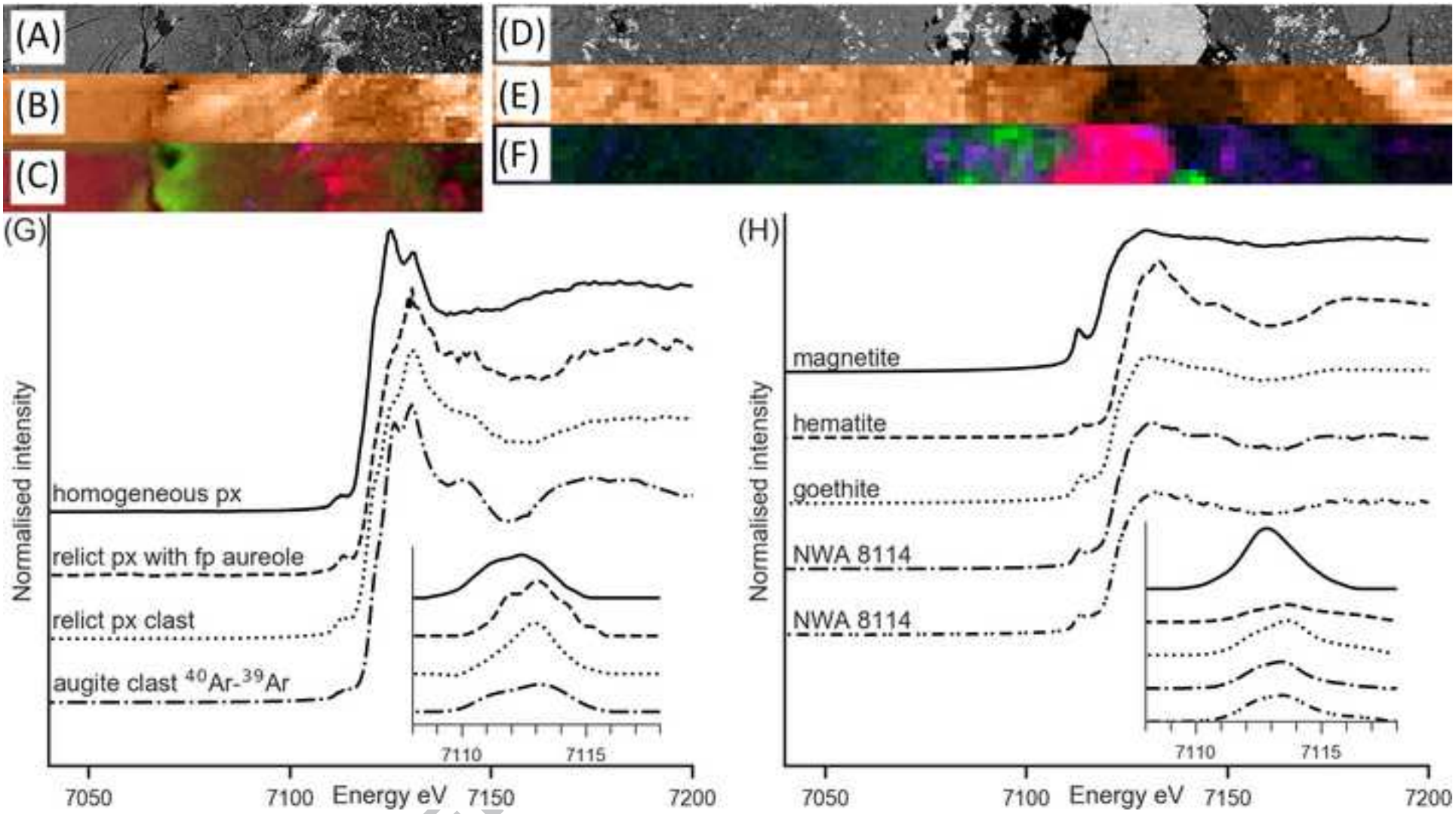

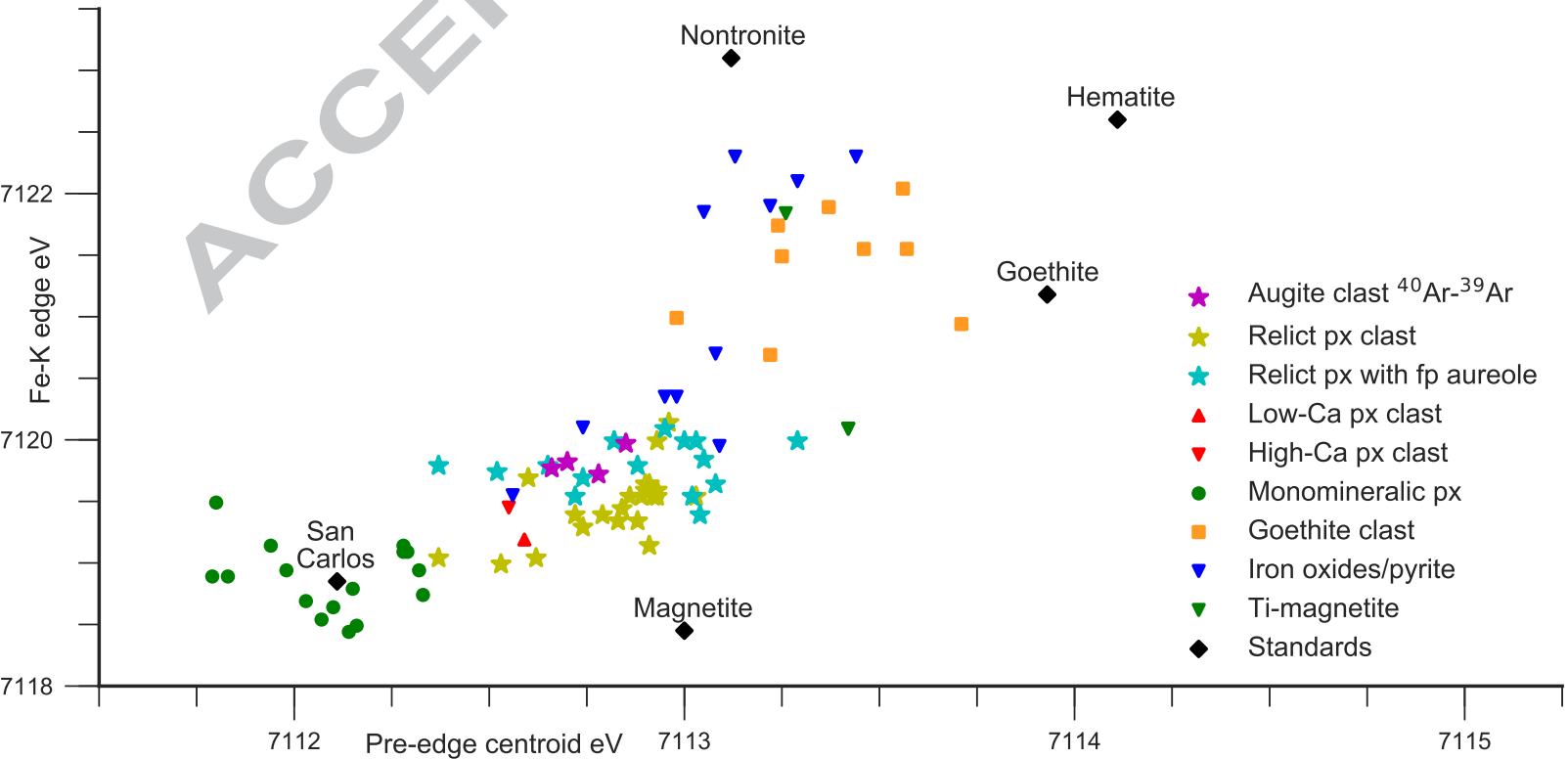

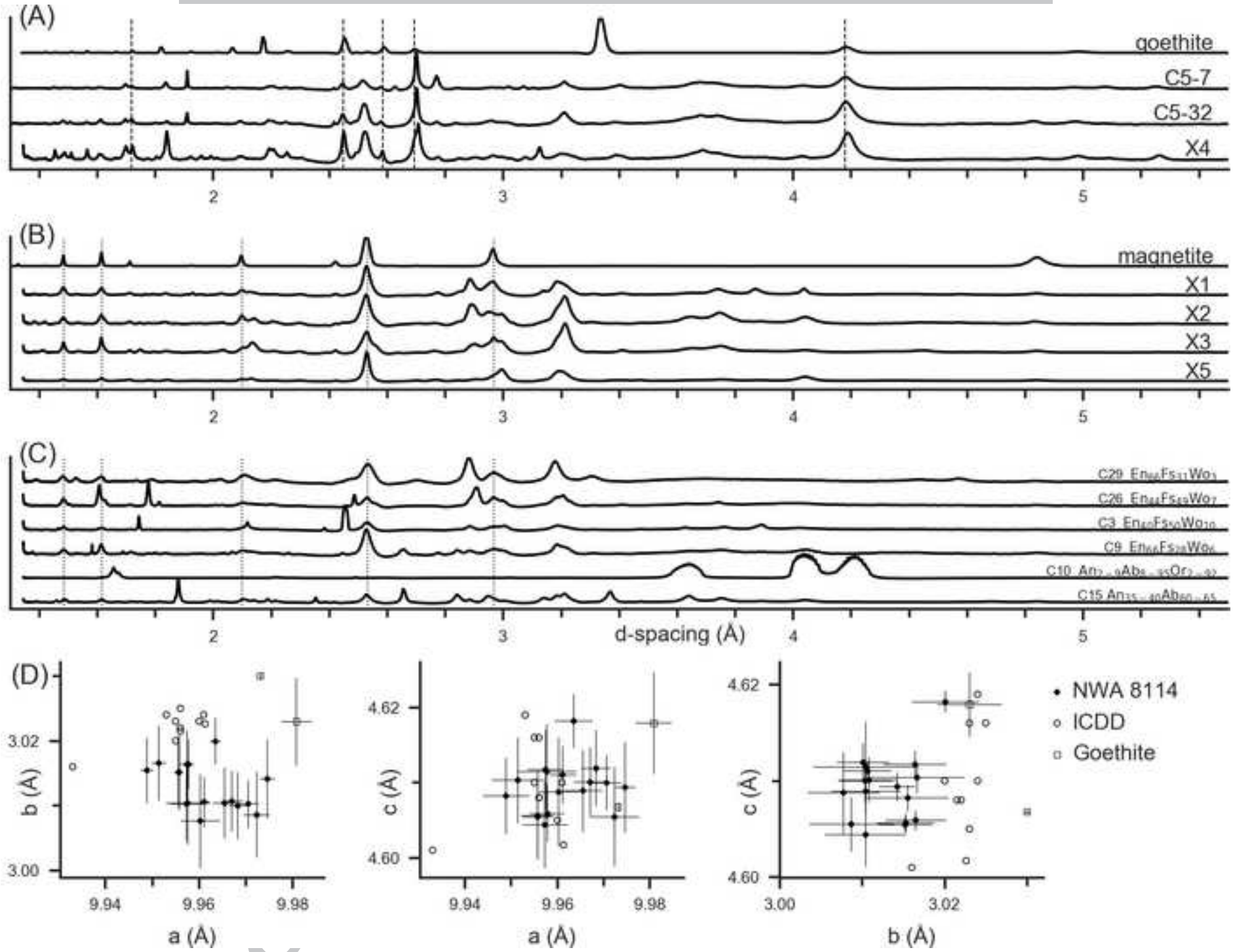

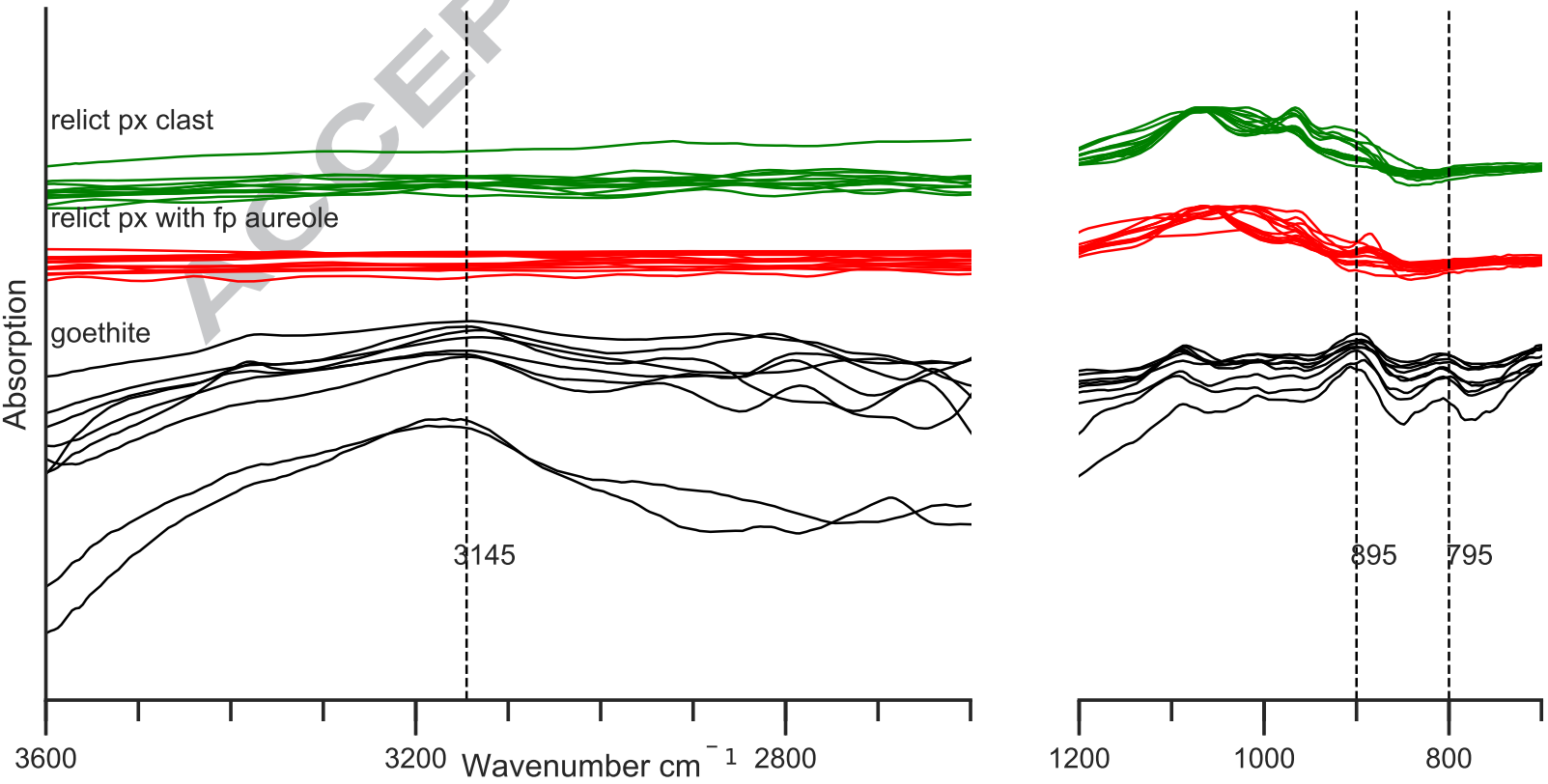

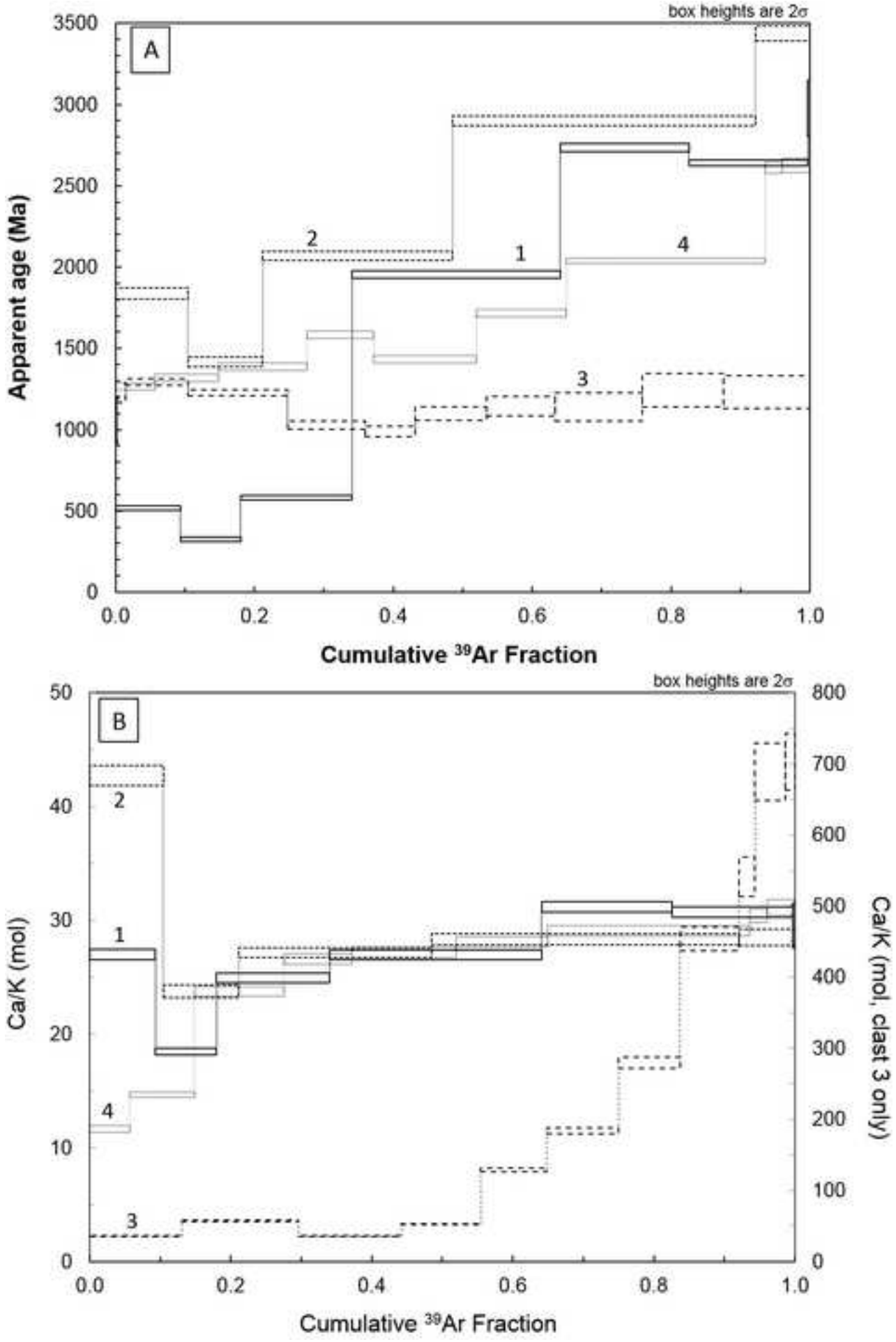

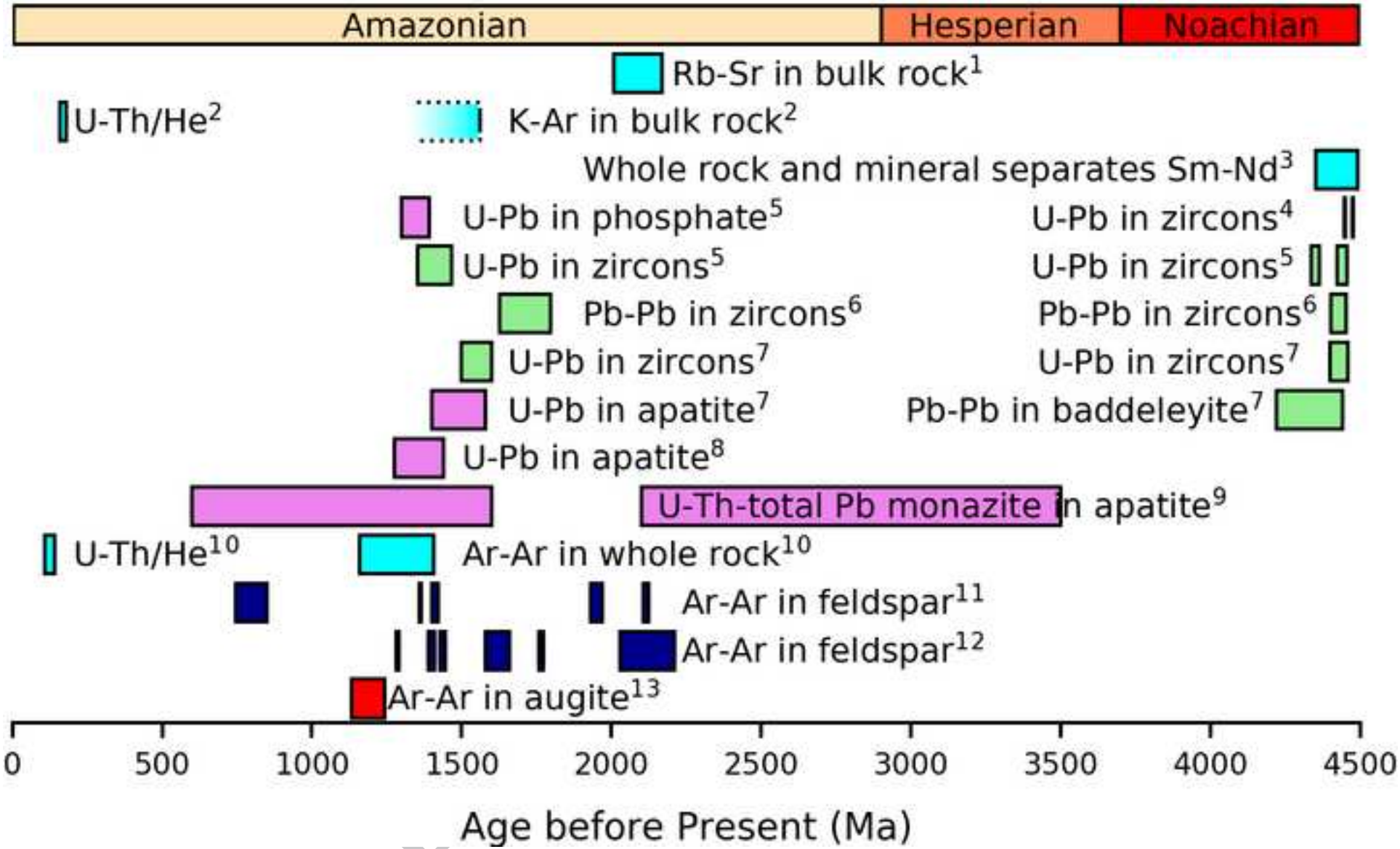

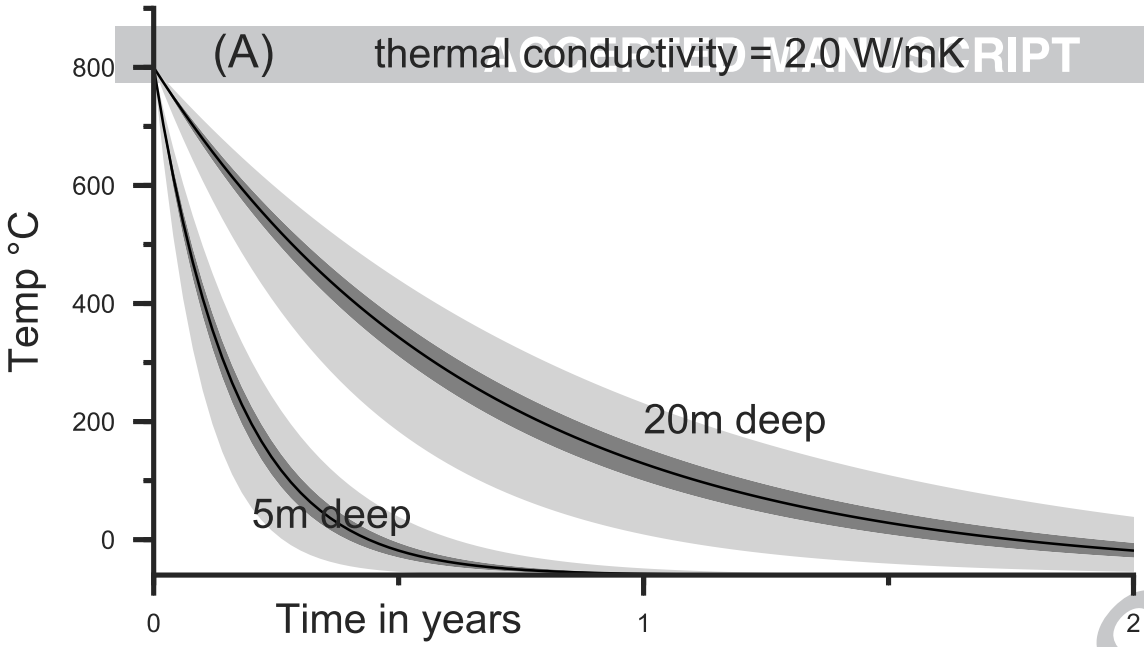

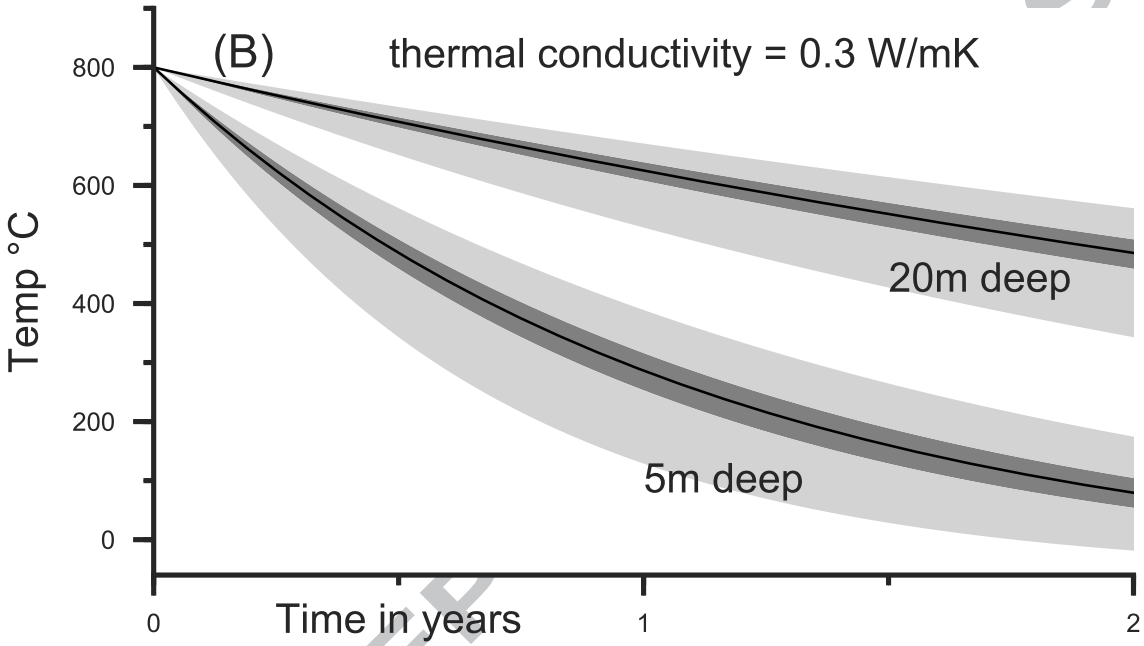

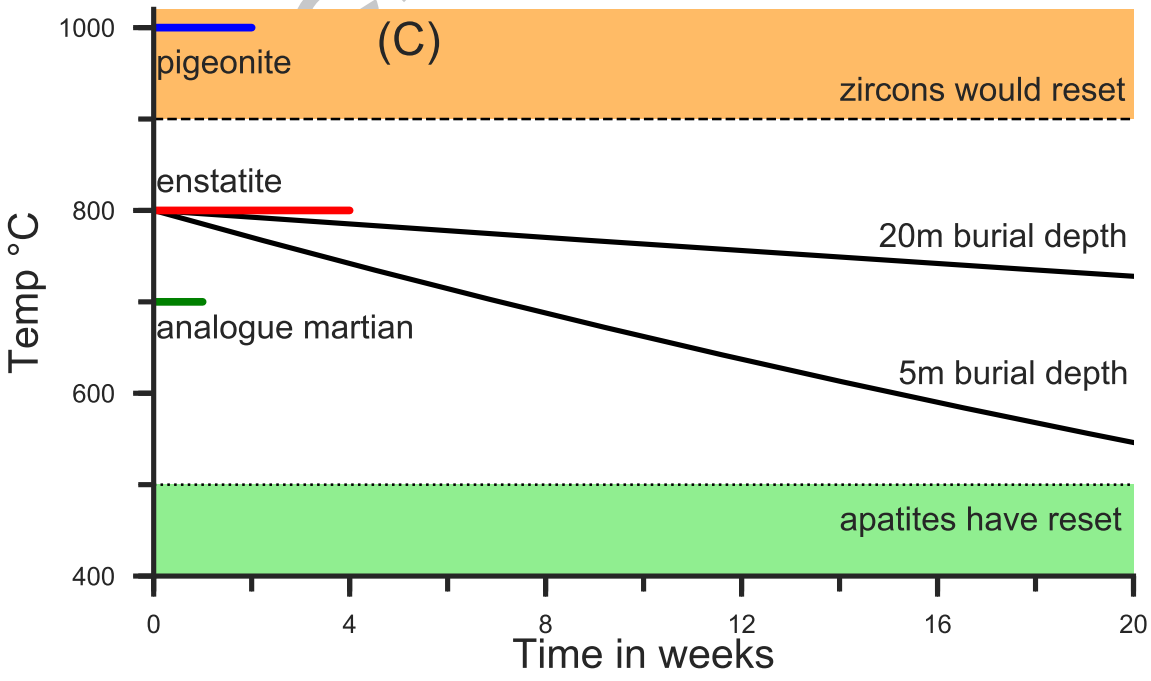

Table 1. Different classifications of clasts within the martian breccias as described by different authors.

Agee et al. (2013)	**Humayun et al. (2013)**	**Santos et al. (2015)**	**Wittmann et al. (2015)**	**Leroux et al. (2016)**	**Hewins et al. (2017)**	**This work**
		Proto-breccia clasts	Sedimentary siltstone clasts		Fine grained sedimentary clasts	
Gabbroic clasts	Fine grained basaltic clasts, microbasalts Lithic plutonic noritic clasts	Basalt clasts Basaltic andesite clasts	Granular & subophitic clasts	Medium- and coarse-grained lithic clasts dominated by magmatic pyroxenes and feldspars	Fine grained basaltic clasts, microbasalts Lithic plutonic noritic clasts, containing inverted pigeonite & exsolution lamellae	
	Lithic plutonic monzonitic clasts	Trachyandesite clasts	Feldspathic clasts		Lithic plutonic monzonitic clasts	
Apatite-ilmenite-alkali feldspar cluster		Fe, Ti, P rich (FTP) clasts	Basalt clasts with ophitic textures of plag, K-spar, ilmenite, chlorapatite		Fe, Ti, P rich (FTP) clasts	
	Lithic leucocratic rock Clast II (NWA 7533-3)		Poikilitic noritic melt clasts			
	Crystal clasts, px and fp	Single mineral fragments	Monomineralic clasts, px and fp fragments		Crystal clasts, px and fp	Monomineralic clasts, px and fp
			Strongly shocked clasts, feldspar & px			Relict pyroxene clasts
Quenched melt clasts and reaction spheres "Plumose" groundmass	Clast-laden impact melt rock (CLIMR), melt rock, melt spherules Impact melt clasts	Melt clasts and reaction spheres	Vitrophyre impact melt clasts, melt shards, melt spherules		Clast-laden impact melt rock (CLIMR), melt rock, melt shards Melt spherules: microcrystalline, vitrophyric and altered	Spherule with accreted rim
					Clump-like aggregates of orthopyroxene surrounded by aureoles of plagioclase (within CLIMR)	Relict pyroxene clasts with feldspar aureole

Px = pyroxene, fp = feldspar, plag = plagioclase, K-spar = potassium feldspar

Table 2: Representative SEM-EDX and EPMA compositions of the relict pigeonite clast with feldspar veins (Fig. 6A), the goethite clast (Fig. 7B), the pyroxene exsolution clast (Fig. 4F) and clasts 1, 2 (plagioclase = plag) and 3 (augite with plagioclase inclusions) dated with ^{40}Ar-^{39}Ar (Fig. 10).

	SEM	**SEM**	**SEM**	**SEM**	**SEM**	**SEM**	**EPMA**	**EPMA**	**EPMA**	**EPMA**	**SEM**	**SEM**	**SEM**	**SEM**
	Vein Fig. 6A1	Vein Fig. 6A2	Clast Fig. 6A3	Vein border: bulk Fig. 6A4	Vein border: light Fig. 6A5	Vein border: dark Fig. 6A6	C5 Goethite Fig. 7B	C5 Goethite Fig. 7B	A103 Pigeonite Fig. 4F	A103 Lamellae Fig. 4F	Clast 1 Zoned plag	Clast 2 Zoned plag	Clast 3 Augite Fig. 10	Clast 3 Plag. Fig. 10F
SiO_2	62.0	64.7	49.1	49.6	47.2	52.8	3.6	1.8	51.7	51.0	56.6	54.5	53.2	67.2
TiO_2	nd	nd	1.3	1.1	1.2	1.2	0.1	0.1	0.2	0.4	nd	nd	nd	nd
Al_2O_3	22.5	19.0	6.4	7.1	4.9	10.5	0.2	nd	0.5	1.5	25.4	25.5	0.9	19.8
Cr_2O_3	nd	nd	nd	nd	nd	nd	nd	nd	0.3	0.8	nd	nd	nd	nd
FeO	1.3	nd	26.4	21.5	24.2	15.4	71.8	73.7	25.1	12.7	nd	nd	9.9	nd
MnO	nd	nd	nd	nd	nd	nd	nd	nd	0.7	0.4	nd	nd	nd	nd
NiO	nd	nd	nd	nd	nd	nd	0.9	0.9	nd	nd	nd	nd	nd	nd
MgO	nd	nd	8.0	10.7	12.0	8.5	0.6	nd	19.5	14.7	nd	0.8	12.0	nd
CaO	5.8	nd	5.6	7.1	9.2	7.6	0.9	0.9	2.2	17.0	9.9	12.4	24.1	2.3
Na_2O	7.2	1.4	0.7	2.4	1.3	3.6	nd	nd	0.1	0.4	7.0	6.7	nd	7.7
K_2O	1.3	14.8	2.5	0.5	0	0.6	nd	nd	nd	nd	1.2	nd	nd	2.9
Total	100.1	99.9	99.9	100.0	100.0	100.2	78.1	77.3	100.3	98.9	100.1	99.9	100.1	99.9
An %	28.6	0.0									41.4	50.6		11.8
Ab %	63.9	12.7									52.8	49.4		70.5
Or %	7.5	87.3									5.8	0.0		17.7
En %					37.3				55.5	43.1			34.4	
Fs %					42.1				40.0	21.0			15.9	
Wo %					20.6				4.5	35.9			49.7	

SEM-EDX given in oxide weight % normalized to 100%.

nd = not detected.

Table 3: Representative TEM-EDX compositions of the pyroxenes studied, given in oxide weight % normalized to 100%.

Clasts:	**Fig. 12A** A140-FIB1	**Fig. 12A** A140-FIB3A	**Fig. 12A** A140-FIB3B	**Fig. 4G** C29-FIB2	**Fig. 4A** B202-FIB6A	**Fig. 4A** B202-FIB6B	**Fig. 4B** B245-FIB7A
SiO_2	49.2	52.9	52.5	53.1	55.1	53.4	54.1
TiO_2	1.0	0.4	0.5	0.8	0.4	0.1	0.4
Al_2O_3	5.6	1.9	3.4	4.8	2.4	4.1	4.4
Cr_2O_3	0.4	0.1	0.1	0.2	0.1	0.1	0.1
FeO	26.6	18.1	12.3	21.0	13.5	6.4	17.0
MnO	0.6	1.0	0.6	0.8	0.8	0.1	0.5
MgO	9.4	19.5	13.2	18.2	26.6	14.9	22.6
CaO	6.9	6.0	17.2	0.9	1.1	20.4	0.7
Na_2O	nd	nd	nd	nd	nd	0.1	nd
K_2O	0.3	0.1	0.2	nd	nd	0.1	nd
P_2O_5	nd	nd	nd	0.3	nd	0.4	0.1
Total	100.0	100.0	100.0	100.1	100.0	100.1	99.9
Number of ions on the basis of 6 oxygens, for pyroxenes.							
Tetrahedral:							
Si	1.91	1.97	1.96	1.95	1.97	1.94	1.95
Al	0.09	0.03	0.04	0.05	0.03	0.06	0.05
Total:	2.00	2.00	2.00	2.00	2.00	2.00	2.00
Octahedral							
Ti	0.03	0.01	0.01	0.02	0.01	0.00	0.01
Al	0.17	0.05	0.11	0.16	0.07	0.12	0.14
Cr	0.01	nd	nd	nd	nd	0.00	0.00
Fe	0.86	0.56	0.38	0.65	0.40	0.19	0.51
Mn	0.02	0.03	0.02	0.02	0.02	0.00	0.01
Mg	0.54	1.08	0.73	1.00	1.42	0.81	1.22
Ca	0.28	0.24	0.69	0.03	0.04	0.80	0.03
Na	nd	nd	nd	nd	nd	0.01	nd
K	0.01	0.01	0.01	nd	nd	0.01	nd
P	nd	nd	nd	0.01	nd	0.01	0.00
Total:	1.92	1.98	1.95	1.89	1.96	1.95	1.92
En %	32.2	57.2	40.6	59.5	76.1	44.9	69.2
Fs %	50.9	30.0	21.2	38.4	21.6	10.8	29.3
Wo %	16.9	12.8	38.2	2.1	2.3	44.3	1.5

Uncertainties on the values are typically 3% for the major elements (Mg, Si, and Ca) and 10% on the minor elements (Al, Ca, Ti, Cr, Mn, and Fe).

nd = not detected.

Table 4: Pre-edge centroid and Fe-K edge energies shown in Fig. 13G, H, and Fig. 14.

Material	Pre-edge centroid energy eV	Fe-K edge energy eV	Material	Pre-edge centroid energy eV	Fe-K edge energy eV
Standards:			Low-Ca px clast (Fig. 4G)	7112.6	7119.2
Hematite (Fig. 13H)	7114.1	7122.6	High-Ca px clast (Fig. 4A)	7112.6	7119.5
Magnetite (Fig. 13H)	7113.0	7118.5	Px clast ^{40}Ar-^{39}Ar (Fig. 10)	7112.7	7119.8
Goethite (Fig. 13H)	7113.9	7121.2	Px clast ^{40}Ar-^{39}Ar (Fig. 10)	7112.9	7120.0
San Carlos olivine	7112.1	7118.9	Px clast ^{40}Ar-^{39}Ar (Fig. 10)	7112.7	7119.8
Nontronite	7113.1	7123.1	Px clast ^{40}Ar-^{39}Ar (Fig. 10)	7112.8	7119.7
NWA 8114:			Relict px (Fig. 2A, Fig. 13A)	7112.9	7119.6
Monomineralic px clasts:			Relict px (Fig. 2A, Fig. 13A)	7112.9	7119.6
104	7112.0	7118.9	Relict px (Fig. 2A, Fig. 13A)	7112.7	7119.3
104	7112.3	7119.1	Relict px (Fig. 2A, Fig. 13A)	7112.8	7119.3
103	7111.9	7119.1	Relict px (Fig. 2A, Fig. 13A)	7112.8	7119.4
26	7111.8	7119.4	Relict px (Fig. 2A, Fig. 13A)	7112.6	7119.7
9	7112.3	7118.7	Relict px (Fig. 2A, Fig. 13A)	7112.9	7119.6
208	7112.3	7119.1	Relict px (Fig. 2A, Fig. 13A)	7112.9	7119.3
130	7112.3	7119.1	Relict px (Fig. 2A, Fig. 13A)	7113.0	7120.1
130	7112.3	7118.9	Relict px (Fig. 2A, Fig. 13A)	7112.9	7119.1
129	7112.1	7118.5	Relict px (Fig. 2A, Fig. 13A)	7112.6	7119.0
129	7112.1	7118.4	Relict px (Fig. 2A, Fig. 13A)	7112.4	7119.0
3	7112.2	7118.5	Relict px (Fig. 2A, Fig. 13A)	7112.9	7119.5
260	7112.0	7118.7	Relict px (Fig. 2A, Fig. 13A)	7112.9	7119.6
260	7112.1	7118.6	Relict px (Fig. 2A, Fig. 13A)	7112.9	7119.5
224	7111.8	7118.9	Relict px (Fig. 2A, Fig. 13A)	7112.9	7120.0
224	7111.8	7118.9	Relict px (Fig. 2A, Fig. 13A)	7112.8	7119.4
209 (Fig. 13G)	7112.2	7118.8	Relict px (Fig. 2A, Fig. 13A)	7112.7	7119.4
Goethite (Fig. 7, Fig. 13H)	7113.5	7121.6	Relict px (Fig. 2A, Fig. 13A)	7112.9	7119.5
Goethite (Fig. 7, Fig. 13H)	7113.6	7121.6	Relict px (Fig. 2A, Fig. 13A)	7113.0	7119.5
Goethite (Fig. 7, Fig. 13H)	7113.2	7121.7	Relict px (Fig. 2A, Fig. 13A)	7112.9	7119.5
Goethite (Fig. 7, Fig. 13H)	7113.4	7121.9	Relict px (Fig. 2A, Fig. 13A)	7112.5	7119.0
Goethite (Fig. 7, Fig. 13H)	7113.0	7121.0	Relict px with aureole (Fig. 7, Fig. 13B)	7113.0	7120.1

Goethite (Fig. 7, Fig. 13H)		7113.3	7121.5	Relict px with aureole (Fig. 7, Fig. 13B)	7113.1	7119.6
Goethite (Fig. 7, Fig. 13H)		7113.6	7122.0	Relict px with aureole (Fig. 7, Fig. 13B)	7112.7	7119.8
Goethite (Fig. 7, Fig. 13H)		7113.2	7120.7	Relict px with aureole (Fig. 7, Fig. 13B)	7113.0	7120.0
Goethite (Fig. 7, Fig. 13H)		7113.7	7120.9	Relict px with aureole (Fig. 7, Fig. 13B)	7113.1	7119.8
Ti-magnetite (Fig. 4C)	114	7113.4	7120.1	Relict px with aureole (Fig. 7, Fig. 13B)	7112.7	7119.7
Ti-magnetite	206	7113.3	7121.8	Relict px with aureole (Fig. 7, Fig. 13B)	7112.8	7120.0
Fe-rich (Fig. 4A)	202	7113.4	7122.3	Relict px with aureole (Fig. 7, Fig. 13B)	7113.0	7119.4
Fe-rich (Fig. 4A)	202	7113.1	7122.3	Relict px with aureole (Fig. 7, Fig. 13B)	7113.0	7119.5
Iron oxide	233	7113.1	7120.7	Relict px with aureole (Fig. 7, Fig. 13B)	7113.0	7120.0
Iron oxide centre	273	7113.0	7120.4	Relict px with aureole (Fig. 7, Fig. 13B)	7113.3	7120.0
Iron oxide edge	273	7113.0	7120.4	Relict px with aureole (Fig. 7, Fig. 13B)	7112.9	7119.8
Iron oxide	267	7113.3	7122.1	Relict px with aureole (Fig. 7, Fig. 13B)	7112.5	7119.7
Fe-rich	267	7113.1	7121.9	Relict px with aureole (Fig. 7, Fig. 13B)	7112.4	7119.8
Fe-rich	206	7113.2	7121.9	Relict px with aureole (Fig. 7, Fig. 13B)	7112.7	7119.5

Table 5: XRD measured *d*-spacings (Å) for indices *hkl*, as plotted in Fig. 15, with calculated unit cell dimensions *a*, *b*, *c* (Å). Measurements from the XRD map in the iron oxide grain (Fig. 7D, black box, C5), XRD point measurements across the relict pyroxene with feldspar aureole showing sub-micron iron oxide grains (Fig. 7A, X1-X5) and the low-Ca relict pyroxene with feldspar aureole showing sub-micron iron oxide grains (C29, Fig. 4G) and reference standards.

Goethite	*a* (Å)	*b* (Å)	*c* (Å)	101	111	301	212	210	511	200	401	201	211	020	610	011	202	500
X4 38913	9.963(4)	3.020(1)	4.618(4)	4.189	2.451	2.704	1.721	2.583	1.565	-	-	-	2.254	1.510	1.455			1.992
C5-7	9.965(5)	3.010(3)	4.609(4)	4.181	2.446	2.701	1.717	2.576	1.563	4.975	2.191	-	2.249	-	-			
C5-32	9.961(4)	3.011(1)	4.611(3)	4.182	2.447	2.701	1.717	2.577	1.564	4.973	2.193	3.386	2.250	1.505	1.453	2.521	2.093	
Goethite[a]	9.981(7)	3.023(3)	4.618(4)	4.184	2.454	2.696	1.721	2.590	1.565	-	2.193	-	-	-	-			
Goethite[b]	9.9613	3.0226	4.6017	4.178	2.449	2.693	1.718	2.584	1.564	4.981	2.190	3.380	2.253	1.511	1.455	2.526		
Goethite[c]	9.956	3.0215	4.608															
Magnetite	*a* = *b* = *c* (Å)			311	440	220	511	400	422	222	111	210	531	441	215	332		
X1 38910	8.389(3)			2.529	-	2.959	1.614	2.099	-	2.422	4.839	-	-	-				
X2 38911	8.391(2)			2.526	-	-	1.615	2.100	1.711	2.424	-	-	1.419	-				
X3 38912	8.376(8)			2.529	1.484	2.968	1.614	-	1.712	2.421	-	-	1.409	-				
X5 38914	8.387(3)			2.529	1.483	-	1.615	2.099	1.710	2.423	4.841	-	-	-				
C29	8.390(10)			2.532	1.488	2.970	1.614								1.526	1.789		
C5-21	8.379(5)			2.519	1.483	2.960	-	2.092		-	4.837	-	-	-				
C5-26	8.353(7)			2.521	-	2.961	-	-		2.420	-	-	-	1.453				
C5-32	8.365(9)			2.521	1.482	-	-	2.093		-	-	-	-	1.453				

C5-50	8.374(2)	2.522	-	2.958	1.612	2.093		2.419	4.840	3.740	-	-
Magnetite[a]	8.3882	2.528	1.483	2.964	-	2.096	1.712	2.421	4.841	-	1.418	-
Magnetite[d]	8.3961	2.532	1.484	2.969	1.616	2.099	1.714	2.424	4.848	-	-	-
Maghemite[e]	8.3364	2.514	1.474	2.947	1.604	2.084	1.702	2.407	4.813	3.728	-	-
Maghemite[c]	8.3474											

Error estimates are given in parentheses and quoted in units of the least significant digit. Unit cell dimension error values calculated from standard deviation.

hkl planes for goethite and magnetite are ordered by intensity per [b] and [d] respectively.

[a] Reference material. [b] Gualtieri et al. (1999) [c] Cornell and Schwertmann (2003) [d] Wechsler et al. (1984) [e] Solano et al. (2014)

[bde] Referenced from American Mineralogical Crystal Structure Database (Downs and Hall-Wallace, 2003).